Research Square

Preprints are preliminary reports that have not undergone peer review.
They should not be considered conclusive, used to inform clinical practice,
or referenced by the media as validated information.

Network-physical coupling technology applicable to distributed energy microgrids and emergency recovery systems in disaster-prone areas

Anjiang Liu

anjiang_liu10@outlook.com

Guizhou Power Grid Co., Ltd

Shuqing Hao

Guizhou Power Grid Co., Ltd

Yue Li

Guizhou Power Grid Co., Ltd

Yu Miao

Guizhou Power Grid Co., Ltd

Hongyu Zuo

Zunyi Normal College

Research Article

Keywords: Agent-based simulation, disaster resilience, microgrids, network-physical coupling, techno-economic optimization, time-series analysis

Posted Date: September 3rd, 2026

DOI: https://doi.org/10.21203/rs.3.rs-10531904/v1

License: This work is licensed under a Creative Commons Attribution 4.0 International License.
Read Full License

Additional Declarations: No competing interests reported.

Network-physical coupling technology applicable to distributed energy microgrids and emergency recovery systems in disaster-prone areas

AnjiangLiu[1,*], Shuqing Hao[2], YueLi[3], Yu Miao[4], HongyuZuo[5]

[1*,2,3,4] Electric Power Research Institute, Guizhou Power Grid Co., Ltd, Guiyang, Guizhou, China

[5] Zunyi Power Supply Bureau of Guizhou Power Grid Company, Zunyi, Guizhou, China

Corresponding Author: AnjiangLiu

Corresponding Author mail: anjiang_liu10@outlook.com

Abstract

Island communities connected to mainland grids face severe risks from natural disasters that damage undersea and overhead transmission lines, resulting in prolonged power outages. This study proposes a network-physical coupling framework for distributed energy microgrids to improve resilience and operational efficiency in disaster-prone regions. Multi-source datasets, including IRENA economic data, CAIDA communication metrics, EM-DAT disaster records, and World Bank regional indicators, are integrated, cleaned, normalized, and aligned with load and renewable generation patterns. HOMER Pro optimization is applied to determine optimal photovoltaic and battery configurations by minimizing Net Present Cost (NPC) and Levelized Cost of Energy (LCOE). A graph-based network-physical model represents electrical and communication infrastructures, enabling topology evaluation, fault propagation analysis, and energy management. MQTT and SCADA protocols simulate real-time communication performance under latency and packet loss conditions, while AC/DC power flow analysis ensures grid stability. Agent-based simulations using AnyLogic evaluate system behavior during normal and disaster scenarios. Results demonstrate improved cost-resilience balance, enhanced reliability, and faster recovery of island microgrids.

Keywords: Agent-based simulation, disaster resilience, microgrids, network-physical coupling, techno-economic optimization, time-series analysis

1. Introduction

Island communities worldwide face persistent challenges in securing reliable and affordable electricity due to their dependence on vulnerable undersea or overhead transmission links to mainland grids [1], [2], [3], [4]. Disruptive events such as storms, earthquakes, and extreme weather frequently damage these connections, leading to prolonged outages that negatively impact healthcare services, economic activities, and overall societal resilience [5], [6]. In many regions, particularly across Indonesian archipelagos, recovery times after such failures remain significantly high, intensifying economic losses and exposing the limitations of centralized energy supply models [7], [8], [9], [10]. Although microgrid-based solutions have emerged as a promising alternative, many existing systems still rely heavily on diesel generation, which increases operational costs, carbon emissions, and fuel dependency while offering limited flexibility during emergencies [11], [12], [13]. The integration of renewable energy sources, especially solar photovoltaic (PV) systems, presents a viable pathway given the high solar potential in tropical island regions; however, widespread adoption is hindered by high initial investment costs and concerns related to intermittency and system stability [14], [15] .Battery energy storage systems play a critical role in mitigating these challenges by enabling energy buffering, peak shaving, and improved reliability, but optimal sizing and operation require comprehensive modeling of load variability, renewable generation uncertainty, and economic trade-offs [16], [17], [18]. Furthermore, recent studies suggest that interconnecting multiple island microgrids into networked configurations can enhance resilience and efficiency by facilitating energy sharing and reducing overall storage requirements, although the effectiveness of such systems depends strongly on load diversity, interconnection capacity, and generation alignment [19], [20], [21].

1.1 Problem statement

Current models of microgrid planning and operation tend to have severe limitations when used in disaster-prone conditions especially where the system is islanded or remote and relies on a vulnerable grid connection. The majority of traditional models, including standalone techno-economic models, are more oriented towards cost optimization and system sizing, but they do not take into account the dynamic processes between the physical power network and the communication (cyber) layer. Consequently, they would not be capturing such critical factors as communication delays, packet losses, and real-time control disruption that would greatly impact

system performance during extreme events. Also, conventional models are not able to model the propagation of faults, energy sharing coordination of networked microgrids, and adaptive decision-making in uncertain disaster conditions. Most of the existing frameworks are also based on fixed or restricted datasets, disregarding the multi-source real-life data (disaster statistics, communication network behavior, etc.) which decreases their practical use.

1.2 Novelty

The originality of this work reflects the physical power system, and, on the other, the communication (cyber) layer of the distributed energy microgrids, which are going to work in disaster-prone zones. In opposition to the traditional strategies that would tend to think solely on the techno-economic optimization, the presented method will integrate multi-source real-world data, such as economic, communication, and disaster-related ones, to develop more realistic and application-oriented model. It proposes a graphical model of microgrid elements and their interactions, which allows performing powerful network topology, fault distribution, and energy routing analysis. The framework also includes communication protocols like MQTT and SCADA in a unique manner to consider latency, packet loss, and delays on control signals that are not usually taken into consideration in the current models. Moreover, the combination of agent-based simulation enables dynamic and autonomous decision-making in normal and disrupted conditions. Resilience-oriented performance evaluation, which employs recovery time, resilience index, communication delay impact, and traditional cost metrics (NPC and LCOE) are also highlighted in the work. Moreover, the capability to model networked microgrid coordination and energy exchange in outages is a major step forward in recovering faster and enhancing system resiliency, unlike alternative microgrid design and analysis tools.

1.3 Contribution

- Analyze the interdependence between physical power systems and communication networks in microgrid operation under both normal and disaster conditions, with emphasis on system resilience and performance variability.
- Apply advanced data preprocessing techniques, including data cleaning, normalization, and time-series alignment, while defining operational constraints related to load demand, resource availability, and economic budget limits.

- Develop a graph-based cyber–physical coupling model to represent microgrid topology, enabling systematic analysis of fault propagation, energy routing mechanisms, and the impact of communication parameters such as latency and packet loss.
- Design an integrated framework that combines HOMER Pro-based techno-economic optimization, AC/DC power flow analysis, and agent-based simulation using AnyLogic to achieve resilient, adaptive, and cooperative microgrid operation in disaster-prone environments.

1.4 Organization of the Paper

The remainder of this paper is organized as follows. Section 2 presents a comprehensive literature survey on microgrid resilience, energy management, and cyber–physical system integration. Section 3 describes the proposed network–physical coupled microgrid framework, including data acquisition, preprocessing, techno-economic optimization using HOMER Pro, graph-based modeling, communication integration, and agent-based simulation. Section 4 discusses the simulation results and performance evaluation in terms of cost, reliability, resilience, and system dynamics under normal and disaster conditions. Finally, Section 5 concludes the paper with key findings, followed by limitations and directions for future research.

2. Literature survey

This section critically examines existing approaches for enhancing resilience and operational performance in network–physical coupled microgrid systems under disaster-prone conditions.

In [22] suggest a resilience-based energy management system on networked microgrids, which considers enhancing the survivability of the system in case of disruptions. The aim is to improve synchronized operation of interconnected microgrids in extreme cases. The authors use an elaborate energy management control plan, which is an optimization-based scheme that is confirmed using a case study in Lombok, Indonesia. The method enhances the resilience of systems through the ability to share power in real-time and speedy fault recovery. The model, however, is based on proper forecasting and communication infrastructure, which can restrict its usability in very uncertain or resource limited environments. The work establishes a basis of resilience-based control measures in the current microgrid platform. Developing the ideas of resilience, [23] discuss the flood-adaptive primary care clinics which operate on smart microgrids and deployable medical technologies. Their aim is to have continuous healthcare delivery in times

of flood disasters. The research combines microgrid design and healthcare infrastructure on the basis of smart energy management and modular deployment methodology. The merit is in the fact that it is interdisciplinary, integrating energy systems and healthcare resilience. Nevertheless, scaling and cost issues might be encountered in the implementation in large areas. This paper expands the use of microgrids in energy systems to essential service continuity.

Equally interested in resiliency in vulnerable areas, [24] study the importance of community microgrids in remote territories in Puerto Rico. They aim to increase energy autonomy and resilience to disasters. The analysis relies on case study and policy examination to show how microgrids are more reliable when localized. The primary strength lies in the focus on community-level solutions and insights on real-world implementation. The weaknesses are however reliance on policy support and funding mechanisms. This article brings out the socio-technical significance of microgrids in disaster-prone areas. Elaborating on the solutions that are decentralized, [25] present mobile solar-biogas hybrid power kiosks, which will improve resilience to disasters. The aim is to offer emergency portable and sustainable energy solutions. The authors create a hybrid energy system that can be deployed on mobile and integrate solar PV and biogas. It has the benefit of being flexible and deploying quickly in off-grid or disaster-impacted locations. The system is however subject to operational difficulties in terms of fuel and maintenance. This article focuses on mobility and hybridization of resilient energy systems. Similarly in mobility, [26] explore the concept of electric trucks as mobile microgrids to serve communities in the form of health clinics. Its aim is to use vehicle-to-grid (V2G) technology in supplying emergency energy. The paper uses an energy informatics model to streamline truck-based microgrids. The positive side is that there is a novel way of utilizing the existing electric vehicle infrastructure to enhance resilience. Nonetheless, it has drawbacks such as battery decay issues and logistics. This paper connects transportation electrification and microgrid resilience.

Towards more sophisticated optimization methods, [27] introduce a Wasserstein distributionally robust optimization model of grid-forming storage in islanded microgrids. The aim is to optimize jointly energy efficiency and uncertainty resilience. The approach uses probabilistic modeling to address the variability of renewables. The benefit is enhanced resilience to unpredictable circumstances. But the model may be computationally complex to be used in real-time. The present research makes contribution to the field of robust optimization in microgrid control.

As a complementary solution to the control strategies, [28] introduces an autonomous decentralized cooperative control model of DC microgrids. It will aim to allow stable operation without central control since batteries are directly connected to the system baseline. The approach uses control coordination algorithms that are decentralized. The benefit is an increase in the reliability of the systems and less dependence on communication. Nevertheless, large networks are not easily scalable or coordinated. This article adds to the paradigm of decentralized control in microgrids. In a larger context, [29] discuss the changing role of smart grids and microgrids in sustainable energy management. It aims at shifting towards strategic energy planning rather than technological solutions only. The conceptual and analytical approach to the study is used to point out trends and integration strategies. Its strengths lie in its holistic approach to energy systems in the future. Nonetheless, it does not have elaborate implementation frameworks. This paper gives a strategic background to the implementation of microgrid technologies.

In response to the issue of security, [30] is interested in planning secure and resilient all-renewable energy grids in smart cities. The aim is to provide cybersecurity and operational stability in renewable dominated systems. The approach entails threat examination and the suggested security structures. The benefit is enhanced protection of the system against cyber-physical attacks. More details on how it is implemented in real-life situations are scarce, however. This article brings out the crucial factor of security in robust microgrid design. Lastly, [31] build a multi-stage stochastic MILP model of renewable microgrid dispatch when the renewable penetration is high. The aim is to handle uncertainty and variability in energy generation. It is a stochastic optimization method of modeling various situations. The benefit is enhanced uncertain decision-making. Nonetheless, the model can be computationally-heavy and reliant on precise probabilistic data. This work reinforces the importance of high order optimization in microgrid power management.

Table 1: Comparative Analysis of Existing Microgrid Energy Management and Resilience Enhancement Strategies

Author & Year	**Objective**	**Method**	**Advantages**	**Disadvantages**

[22]	Enhance resilience of networked microgrids under disruptions	Optimization-based coordinated energy management framework	Improves system recovery and adaptive power sharing	Requires accurate forecasting and strong communication network
[23]	Ensure uninterrupted healthcare during floods	Smart microgrid integration with modular energy management system	Supports critical healthcare services; adaptive design	High cost and scalability challenges
[24]	Improve resilience in remote communities	Community-based microgrid architecture with distributed energy resources (DERs)	Enhances local reliability and energy independence	Depends on regulatory and financial support
Tsegaye et al., [25]	Provide portable energy during disasters	Hybrid solar–biogas energy system with mobile deployment design	Renewable, flexible, and rapidly deployable	Fuel logistics and maintenance complexity
Wang et al., [26]	Utilize EVs as mobile microgrids	Vehicle-to-grid (V2G) energy management and scheduling framework	Efficient use of EV storage for emergency supply	Battery degradation and operational constraints

Shao et al., [27]	Optimize resilience under uncertainty	Wasserstein distributionally robust optimization (WDRO)	Strong uncertainty handling and robustness	High computational burden
Yamada, [28]	Enable stable decentralized DC microgrid control	Autonomous decentralized cooperative control algorithm	Reduces communication dependency; improves stability	Limited scalability for large systems
Lu and Le, [29]	Provide strategic insight on smart grids	Integrated energy management and planning framework	Holistic and future-oriented approach	Lacks technical implementation depth
Konstantinou, [30]	Ensure cybersecurity in renewable grids	Cyber-physical security framework for smart grids	Enhances protection against cyber threats	Limited real-world validation
Babatunde et [31]	Optimize microgrid dispatch under uncertainty	Multi-stage stochastic mixed-integer linear programming (MILP)	Handles renewable variability effectively	Computationally intensive and data-dependent

Table 1 illustrates Comparative Analysis of Existing Microgrid Energy Management and Resilience Enhancement Strategies. Although the field of microgrids has made tremendous progress, there are still some important gaps to fill to enable the realization of fully resilient and adaptive energy systems. The current literature is either about optimization-oriented energy management or decentralized control without a common framework that can be used to combine resilience, real-time adaptability, and multi-source coordination during extreme conditions. Although methods like Wasserstein distributionally robust optimization can treat uncertainty, they are computationally expensive and thus cannot be implemented in real-time. Equally, mobile and community-based microgrids solutions enhance flexibility, but tend to ignore a smooth transition

control, power quality challenges, and dynamic load changes. Additionally, numerous researches require a strong communication system and effective predictions, which cannot be attained in disaster-affected or isolated areas. Practical deployments are also poorly covered in terms of cybersecurity and scalability. Thus, the necessity to have a computationally efficient, robust, and integrated control strategy that provides smooth operation, improved power quality, and robust performance of microgrids in highly uncertain and dynamic situations is obvious.

3. Proposed Methodology

The suggested methodology includes a holistic network-physical coupling model of resilient microgrid operation in disaster prone settings. It starts with a multi-source data collection, which combines economic data provided by IRENA, communication network data provided by CAIDA, and disaster and outage data provided by EM-DAT, and regional indicators offered by the World Bank. The gathered data are subsequently pre-treated with cleaning, normalization, and alignment of load demand and renewable generation profiles with time-series after which the constraint is formed using demand, resource availability, and budget constraints. HOMER Pro is used to carry out a techno-economic optimization to identify an optimal PV and battery sizing with goals to minimize NPC and LCOE and to provide reliable power supply. A graph-based network-physical coupling model is further used to model the system, where nodes represent generation, storage and load units, and edges model electrical and communication connections, allowing topology, fault propagation and energy routing to be studied. MQTT and SCADAR protocols are integrated into the communication layer to model an actual control behavior in the presence of latency and packet loss, and stability of the system is provided by analysis of AC/DC power flows. A dynamic interaction between the components of a microgrid is simulated using Any logic models in an agent-based simulation in both regular and disaster conditions. Figure 1 illustrates Block diagram of the proposed model.

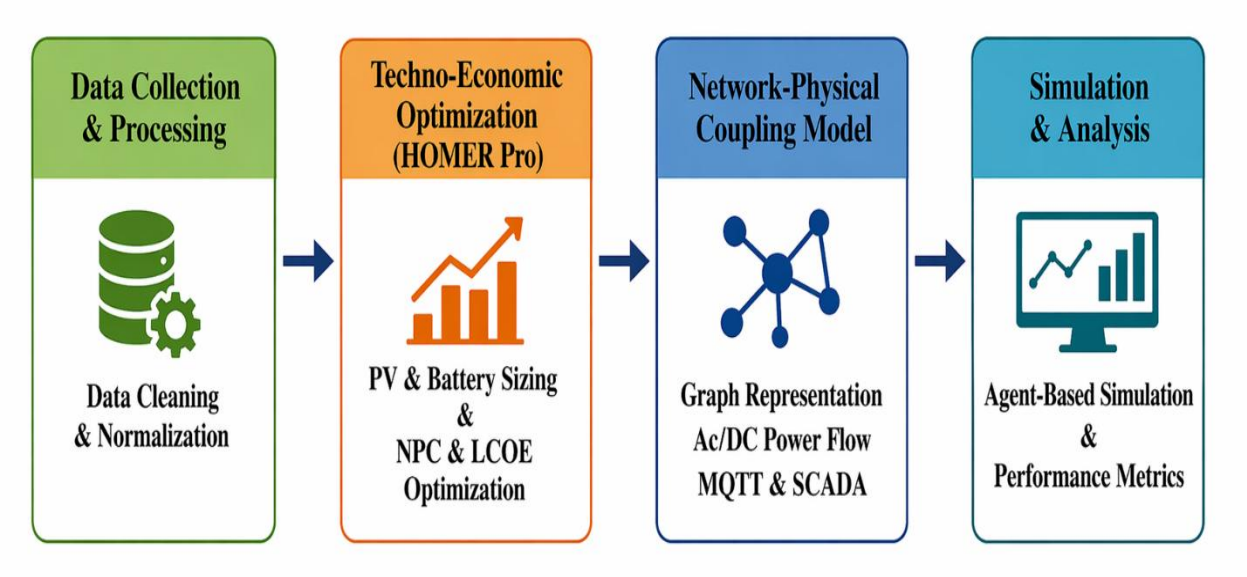


Figure 1: Block diagram of the proposed model

3.1 Network–Physical Coupled Microgrid Framework and Operational Strategy

This subsection presents the integrated framework for modeling and operation of a network–physical coupled microgrid system based on multi-source datasets and hybrid simulation tools. The proposed methodology begins with the acquisition of heterogeneous datasets, including techno-economic parameters such as system cost, component lifetime, and maintenance cost from the IRENA dataset; communication network characteristics such as latency, bandwidth, and packet loss from the CAIDA dataset; disaster and outage statistics from the EM-DAT dataset; and regional socio-economic indicators from the World Bank dataset. These datasets collectively enable a comprehensive representation of both the physical power system and the cyber communication infrastructure. Figure 2 illustrates Schematic diagram of microgrids under normal operation (top) and under networked microgrid configuration under emergency conditions (bottom).

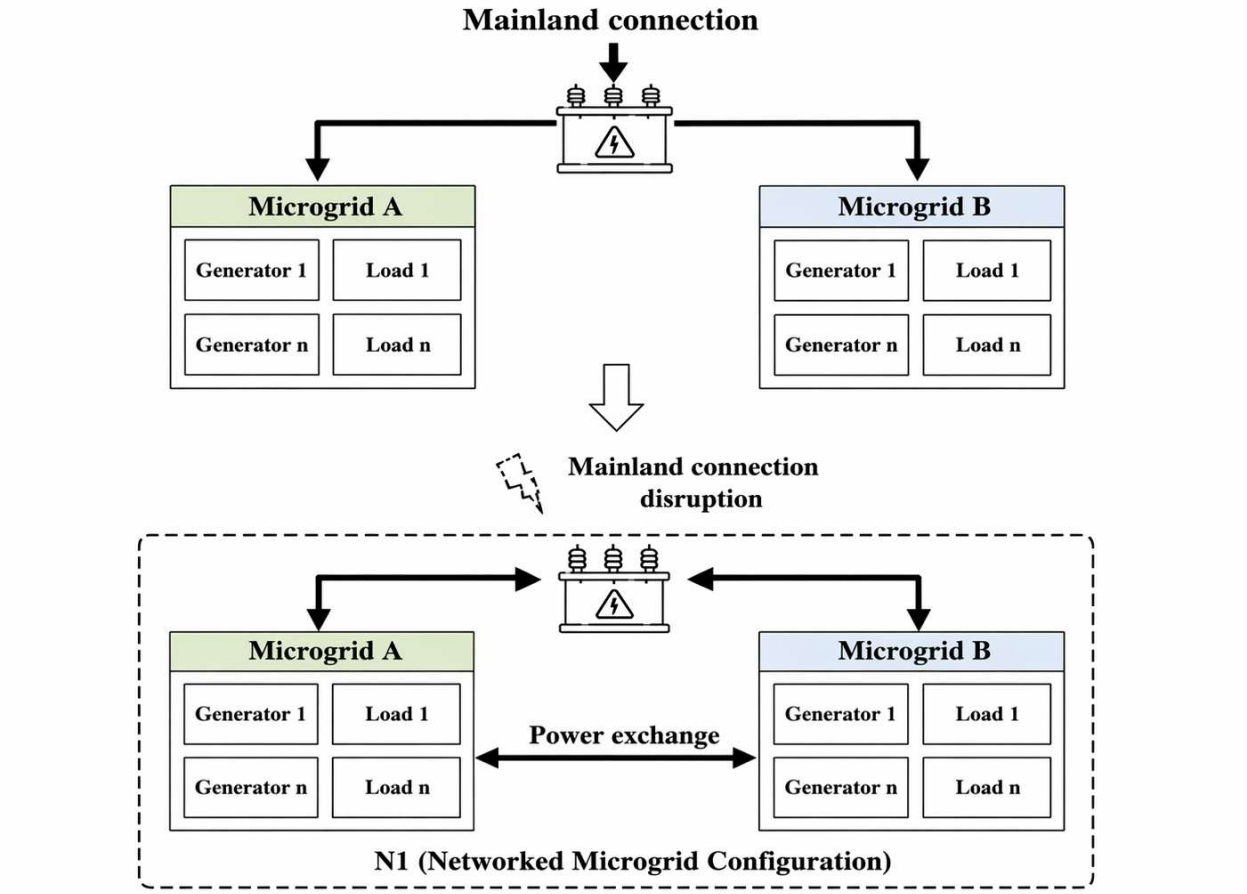


Figure 2: Schematic diagram of microgrids under normal operation (top) and under networked microgrid configuration under emergency conditions (bottom)

The acquired datasets are subjected to a structured preprocessing stage involving data cleaning, normalization, and time-series alignment. Let $X_i(t)$denote the raw data from source i. The normalized dataset $X_i^{norm}(t)$is obtained in equation (1)

$$X_i^{norm}(t) = \frac{X_i(t)-\mu_i}{\sigma_i} \quad (1)$$

where $\mu_i$and $\sigma_i$represent the mean and standard deviation of dataset i. Time-series alignment ensures synchronization between load demand $P_L(t)$and renewable generation $P_{RES}(t)$, which is essential for consistent system simulation. Following preprocessing, techno-economic optimization is performed using HOMER Pro to determine the optimal sizing of photovoltaic (PV) generation and BESS. The optimization objective is to minimize the NPC and LCOE, expressed in equation (2,3).

$$NPC = \sum_{t=0}^{T} \frac{C_t}{(1+r)^t} \tag{2}$$

$$LCOE = \frac{\sum_{t=0}^{T} \frac{C_t}{(1+r)^t}}{\sum_{t=0}^{T} \frac{E_t}{(1+r)^t}} \tag{3}$$

where $C_t$is the total cost in year t, $E_t$is the energy supplied, $r$is the discount rate, and $T$is the project lifetime. The optimized PV capacity $P_{PV}$and storage capacity $E_{BESS}$are then used as inputs for further system modeling. To capture the interdependency between cyber and physical layers, the microgrid is modeled as a graph $G = (V, E)$, where nodes Vrepresent system components such as generators, loads, storage units, and controllers, while edges Erepresent electrical and communication links. The power flow constraint across the network is given in equation (4).

$$P_i - P_j = \frac{V_i V_j}{X_{ij}} \sin(\theta_i - \theta_j) \tag{4}$$

where V_i, $V_j$are bus voltages, $X_{ij}$is line reactance, and θ_i, $\theta_j$are voltage angles. This formulation supports topology analysis, energy routing, and fault propagation studies. The communication layer is modeled using MQTT–SCADA protocols to simulate real-time monitoring and control under network uncertainties. The impact of latency $\lambda$and packet loss probability $p$on control signal delivery can be expressed in equation (5).

$$D_{eff}(t) = D(t - \lambda) \cdot (1 - p) \tag{5}$$

where $D(t)$represents the original control signal and $D_{eff}(t)$is the effective received signal. This formulation highlights the degradation of control performance under adverse communication conditions. Finally, an agent-based simulation framework in AnyLogic is employed to capture dynamic interactions among system components, including loads, renewable generators, storage units, and controllers. The system power balance under both normal and disaster scenarios is maintained in equation (6).

$$P_{PV}(t) + P_{BESS}(t) + P_{grid}(t) = P_L(t) + P_{loss}(t) \tag{6}$$

where $P_{BESS}(t)$represents battery charge/discharge power and $P_{loss}(t)$denotes system losses. This dynamic modeling approach enables the evaluation of system resilience, reliability, and adaptive response under varying operating conditions. Overall, the proposed framework integrates data-driven optimization, graph-based modeling, and cyber-physical simulation to provide a robust platform for analyzing microgrid performance, fault tolerance, and energy management in both normal and extreme scenarios.

3.2 Data acquisition

This section shows the datasets used in the study, describing the sources, structure, and key characteristics of each dataset, including CAIDA for network topology, IRENA for renewable energy statistics, World Bank for socio-economic indicators, and EM-DAT for global disaster records.

3.2.1 CAIDA dataset

CAIDA dataset is gathered by use of the Border Gateway Protocol (BGP) routing table snapshots of the University of Oregon Route Views project. It has 122 network graphs on Autonomous System (AS) relationship of the Internet over time. The largest instance of the graph has about 26,475 nodes and 106,762 edges. The graphs are all Internet AS-level connectivity graphs, with nodes (autonomous systems) and edges (relationships between nodes based on routing). The data mainly contains the characteristics of graph topology (nodes, connectivity, edges, clustering, diameter, shortest paths).

3.2.2 IRENA dataset

The data used in the IRENA database is gathered in International Renewable Energy Agency, official database of global energy statistics. It has country-level statistics of renewable energy and electricity over several years. The data involves about 200 or more countries/regions, and 30 or more years of time-series data, which makes thousands of observations (country-year combinations). Its content has indicators like installed renewable capacity (solar, wind, hydro, bioenergy), electricity production, investment, and energy balance measures.

3.2.3 World Bank Dataset

This data comes via the World Bank Open Data database that is a compilation of global social-economic and development indicators gathered through national statistics bureaus and

international surveys. It contains information on more than 200 countries over a number of decades. Data set has thousands to millions of records based on the indicators chosen as there are numerous time-series variables. They are GDP, population, inflation, literacy rate, access to electricity, CO2 emission, health indicators, and other development indicators.

3.2.4 EM-DAT Dataset

This dataset is grounded on the EM-DAT at the Centre of Research on the Epidemiology of Disasters (CRED). It holds the world records of natural and technological disasters reported throughout the world. Depending on the version, the dataset contains about more than 20,000-25,000 records of disaster events. Every record shows the disaster like floods, earthquakes, storms, droughts and epidemics. The main characteristics are disaster type and sub-type, country, start/end date, affected people, fatalities, injuries, economic losses and place of occurrence.

3.3 Data Preprocessing for Network–Physical Coupled Microgrid System

The acquired datasets from IRENA, CAIDA, EM-DAT, and World Bank are subjected to a structured preprocessing pipeline to ensure consistency, comparability, and suitability for time-series based microgrid analysis. The preprocessing consists of six sequential stages as follows.

The first stage addresses missing value treatment in raw time-series data, which commonly arises due to sensor failures, reporting delays, or communication losses across distributed datasets. To maintain continuity, missing values are estimated using either linear interpolation or statistical substitution. For a time-series variable x_t, the imputed value is defined in equation (7).

$$x_t = \begin{cases} \frac{x_{t-1}+x_{t+1}}{2}, & \text{if interior missing value} \\ \mu_x, & \text{if boundary or extended missing segment} \end{cases} \quad (7)$$

Where, μ_x is the mean of available observations. This ensures that temporal trends are preserved without introducing abrupt discontinuities, which is essential for stable microgrid forecasting and dynamic modeling. The fifth stage standardizes network performance indicators such as latency, bandwidth, and packet loss using Z-score normalization to ensure statistical comparability. This is particularly important for CAIDA-based communication network data where distributional characteristics vary significantly. The standardized form is defined in equation (8).

$$z_t = \frac{x_t - \mu}{\sigma} \quad (8)$$

Where, μ is the mean and $\sigma$is the standard deviation. This scaling ensures that all features contribute equally during optimization and machine learning processes, preventing dominance of high-magnitude variables and improving convergence behavior in coupled system simulations. The third stage focuses on time-series alignment, as the datasets originate from different temporal resolutions such as hourly, daily, and yearly records. To ensure consistency, all datasets are resampled onto a unified time index using interpolation or aggregation functions depending on data granularity. The alignment operation is expressed in equation (9).

$$X_{\text{aligned}}(t) = f(X_{IRENA}(t), X_{CAIDA}(t), X_{EM-DAT}(t)) \tag{9}$$

Where,$X_{\text{aligned}}(t)$ is the unified time-aligned dataset at time t, obtained by applying the fusion function $f(\cdot)$ to combine energy data $X_{\text{IRENA}}(t)$, communication network data $X_{\text{CAIDA}}(t)$, and disaster/outage data $X_{\text{EM-DAT}}(t)$. This step is critical for synchronizing energy, network, and disaster-related dynamics within a single coherent temporal framework. The fourth stage maps load demand and renewable energy generation profiles to evaluate system balance at each time step. This enables accurate representation of microgrid operational conditions under varying renewable penetration levels. The net power balance is computed in equation (10).

$$P_{net}(t) = P_{\text{load}}(t) - (P_{\text{solar}}(t) + P_{\text{wind}}(t)) \tag{10}$$

The fifth stage involves data normalization to eliminate scale disparities among economic, energy, and communication network variables. Since datasets such as cost, latency, and power generation operate in different numerical ranges, Min–Max scaling is applied to map all variables into a unified interval. The transformation is given in equation (11).

$$x_t^{norm} = \frac{x_t - x_{\min}}{x_{\max} - x_{\min}} \tag{11}$$

This transformation centers the data around zero with unit variance, improving robustness in network–energy co-simulation and reducing bias from extreme network fluctuations. The final stage involves outlier detection and smoothing to eliminate anomalous values caused by sensor noise, rare disturbances, or data transmission errors. Outliers are identified using the Interquartile Range (IQR) method, defined in equation (12).

$$IQR = Q_3 - Q_1 \tag{12}$$

Detected outliers are replaced using a moving average filter, expressed in equation (13).

$$x_t^{\text{smooth}} = \frac{1}{k}\sum_{i=t-k}^{t} x_i \quad (13)$$

This ensures a smooth and physically realistic dataset, preserving underlying trends while removing abrupt distortions, thereby enhancing the reliability of subsequent microgrid resilience and optimization analysis.

3.4 Techno-economic optimization using HOME pro

HOMER Pro is a widely used techno-economic optimization tool for designing and evaluating hybrid energy systems, particularly microgrids integrating renewable energy sources and storage systems. It enables the simulation of various system configurations by combining photovoltaic (PV) generation, battery energy storage systems (BESS), and grid or backup supply options. The software evaluates each configuration based on technical feasibility and economic performance over the project lifetime. In this work, HOMER Pro is employed to determine the optimal sizing of PV panels and battery storage systems to ensure reliable power supply while minimizing economic indicators such as Net Present Cost (NPC) and Levelized Cost of Energy (LCOE). Figure 3 illustrates Workflow for Optimal Sizing of PV and Battery System Using HOMER Pro.

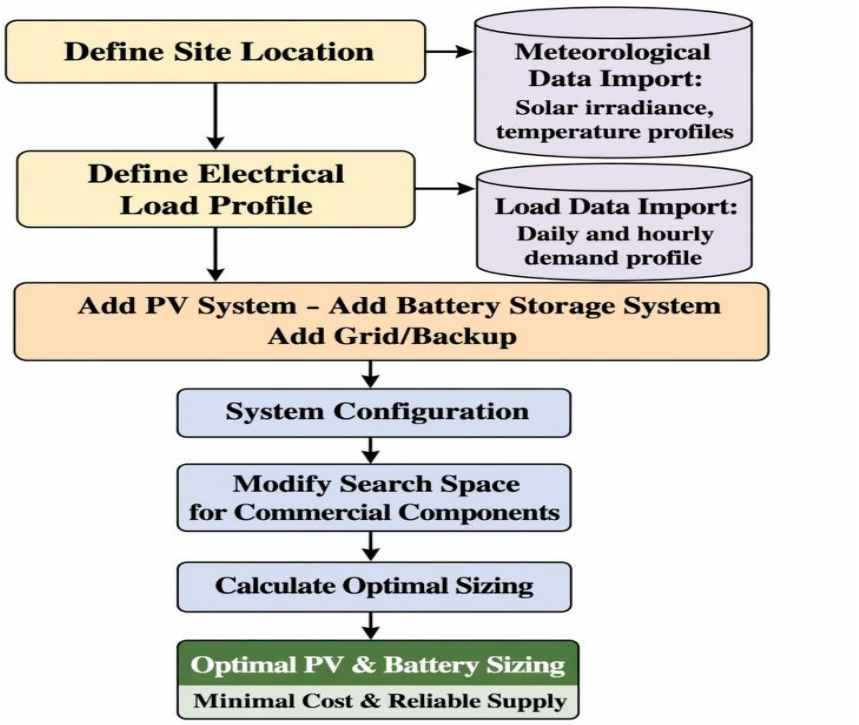


Figure 3: Workflow for Optimal Sizing of PV and Battery System Using HOMER Pro

A. Sizing Methodology Description

The optimal sizing process using HOMER Pro follows a structured workflow. First, the geographical location of the system is defined using latitude and longitude coordinates. This enables HOMER to import site-specific solar irradiance, temperature profiles, and other meteorological data required for accurate PV generation modeling. Next, the electrical load profile is defined based on the daily and hourly demand characteristics of the target system. The load may include residential, commercial, or critical infrastructure demand, and small stochastic variations (typically within ±10%) may be introduced to reflect realistic uncertainty in consumption patterns. Following load definition, the system components are configured. This includes the PV array as the primary generation source and the battery storage system for energy balancing and reliability enhancement. Each component is defined using technical parameters such as rated capacity, efficiency, lifetime, and operational constraints, along with economic parameters including capital cost, replacement cost, and maintenance cost. HOMER Pro then performs iterative simulations across a wide range of PV and battery size combinations. For each configuration, the system is evaluated under hourly time-step simulation to ensure load demand is met while accounting for renewable variability and storage dynamics. The optimization tool identifies feasible configurations that satisfy load requirements and selects the optimal solution based on minimum NPC and LCOE.

B. Economic Modeling and Objective Function

The techno-economic optimization in HOMER Pro is primarily driven by the minimization of Net Present Cost (NPC), which represents the total lifecycle cost of the system. NPC is expressed in equation (14).

$$NPC = \frac{C_{TA}}{CRF(d,n)} \tag{14}$$

Where, $C_{TA}$is the total annualized cost, $d$is the discount rate, and $n$is the project lifetime in years. The Capital Recovery Factor (CRF) is defined in equation (15).

$$CRF(d,n) = \frac{d(1+d)^n}{(1+d)^n-1} \tag{15}$$

NPC aggregates all system costs including capital investment, replacement, operation and maintenance (O&M), converted into present value over the project lifetime. In addition to NPC,

the Levelized Cost of Energy (LCOE) is used as a key performance indicator to assess the cost-effectiveness of the system. LCOE represents the average cost of producing one unit of electrical energy and is defined in equation (16).

$$LCOE = \frac{C_{TA}}{E_{served}} \tag{16}$$

where, $E_{served}$is the total electrical energy supplied to the load over the project lifetime.

3.5 Graph-Based Cyber–Physical Coupling Framework for Topology Analysis, Fault Propagation and Energy Routing in Microgrids

In this work, the network–physical coupling of the microgrid is represented using a graph-theoretic formulation that unifies both electrical power interactions and communication/control dependencies within a single mathematical framework. The graph-based cyber–physical coupling framework models the microgrid as an integrated system in which electrical energy flow and communication-based control interactions are jointly represented through a unified mathematical structure. The system is formulated as a directed weighted graph $G(t) = (V, E(t))$, where Vdenotes the set of nodes corresponding to physical components such as photovoltaic units, wind generators, battery storage systems, loads, grid interfaces, and control devices, while $E(t)$represents time-dependent edges capturing both electrical power transfer and communication links. The time dependency reflects the dynamic nature of microgrid operation under varying load, renewable generation, and fault conditions. Each edge $(i, j) \in E(t)$is assigned a composite weight that integrates electrical, communication, and reliability characteristics, expressed in equation (17).

$$w_{ij}(t) = \alpha\, w_{ij}^{elec} + \beta\, w_{ij}^{comm} + \gamma\, w_{ij}^{risk}(t) \tag{17}$$

where w_{ij}^{elec}represents electrical parameters such as line impedance or power transfer capacity, w_{ij}^{comm}denotes communication attributes such as latency or packet loss, and $w_{ij}^{risk}(t)$captures time-varying failure probability derived from historical outage data. The coefficients $\alpha, \beta, \gamma$are weighting factors that balance the relative influence of physical and cyber layers. The connectivity of the cyber–physical network is represented using a weighted adjacency matrix $A(t) \in \mathbb{R}^{n \times n}$, defined in equation (18).

$$A_{ij}(t) = \begin{cases} w_{ij}(t), & \text{if a connection exists between nodes } i \text{ and } j \\ 0, & \text{otherwise} \end{cases} \quad (18)$$

The operational behavior of the microgrid is governed by nodal power balance equations that incorporate the influence of optimized generation and storage sizing obtained from HOMER Pro. For each node i, the balance is expressed in equation (19).

$$P_i^{gen}(t) + P_i^{grid}(t) + P_i^{storage}(t) = P_i^{load}(t) + \sum_{j \in V} P_{ij}(t) \quad (19)$$

where $P_{ij}(t)$represents the power flow between interconnected nodes, constrained by line capacity and system limits. This formulation ensures that energy conservation is maintained while embedding network interactions directly into system operation. Topology analysis is carried out using graph-theoretic metrics that quantify structural importance and system resilience. The degree of node i, given in equation (20).

$$k_i = \sum_j A_{ij}(t) \quad (20)$$

$A_{ij}(t)$ indicates its level of connectivity and influence within the network. The efficiency of both energy delivery and communication signaling is evaluated through the weighted shortest path between nodes $i$and j, defined in equation (21).

$$d(i,j) = \min \sum_{(m,n) \in \mathcal{P}} w_{mn}(t) \quad (21)$$

where $\mathcal{P}$denotes all feasible paths. This formulation inherently captures the trade-off between electrical losses and communication delays. The criticality of nodes in maintaining system connectivity is further assessed using betweenness centrality, expressed in equation (22).

$$C_B(v) = \sum_{s \neq v \neq t} \frac{\sigma_{st}(v)}{\sigma_{st}} \quad (22)$$

where $\sigma_{st}$is the total number of shortest paths between nodes $s$and t, and $\sigma_{st}(v)$represents those paths passing through node v. Nodes with high centrality values are identified as critical for both power transfer and control signal routing. Fault propagation within the cyber–physical network is modeled as a time-dependent degradation of connectivity influenced by external disturbances such as natural disasters. Instead of binary disconnection, failures are incorporated probabilistically

using a fault function $F_{ij}(t) \in [0,1]$, leading to an updated adjacency representation is shown in equation (23).

$$A_{ij}(t) = w_{ij}(t)\big(1 - F_{ij}(t)\big) \tag{23}$$

where increasing values of $F_{ij}(t)$reduce the effective strength of the connection and may eventually lead to disconnection. This enables the simulation of cascading failures, where disruptions in one part of the network propagate through both electrical and communication layers. Energy routing in the microgrid is formulated as an optimization problem over the graph, where the objective is to determine the optimal set of paths that minimize overall system cost while ensuring reliable supply. This is expressed in equation (24).

$$\mathcal{P}^* = \arg\min_{\mathcal{P}} \sum_{(i,j)\in\mathcal{P}} w_{ij}\,(t) \tag{24}$$

The resulting routing strategy ensures efficient energy distribution under both normal and disrupted conditions. The dynamic interaction of nodes, including adaptive responses of loads, generators, storage units, and controllers, is further evaluated through agent-based simulation using Any Logic, where the evolving graph $G(t)$serves as the underlying structural backbone for analyzing system performance during both steady-state and disaster scenarios.

3.6 Cyber–Communication Modeling Using MQTT–SCADA Integration

The cyber layer of the proposed network–physical microgrid is modeled through a MQTT–SCADA architecture to realistically capture real-time monitoring, control actions, and communication imperfections such as latency and packet loss.

Figure 4 illustrates MQTT- SCADA system data flow and control architecture. Where, distributed publisher nodes (PV units, battery systems, loads, and control agents) continuously generate and transmit real-time operational data such as voltage, current, power, and frequency to an MQTT broker over a public network subject to latency (τ_net) and packet loss (λ). The broker manages topic-based data routing with hierarchical addressing (e.g., microgrid/pv, battery, load, control) and supports different Quality of Service (QoS 0, 1, 2) levels to ensure appropriate delivery guarantees, including retransmissions when required. The communication model incorporates delay-aware message reception and probabilistic reliability, where successful delivery depends on retransmission attempts under packet loss conditions. On the subscriber side, the SCADA system

receives processed data streams for real-time monitoring, visualization, alarm handling, and supervisory decision-making, while also issuing control commands and setpoints back through the broker to actuators in the microgrid.

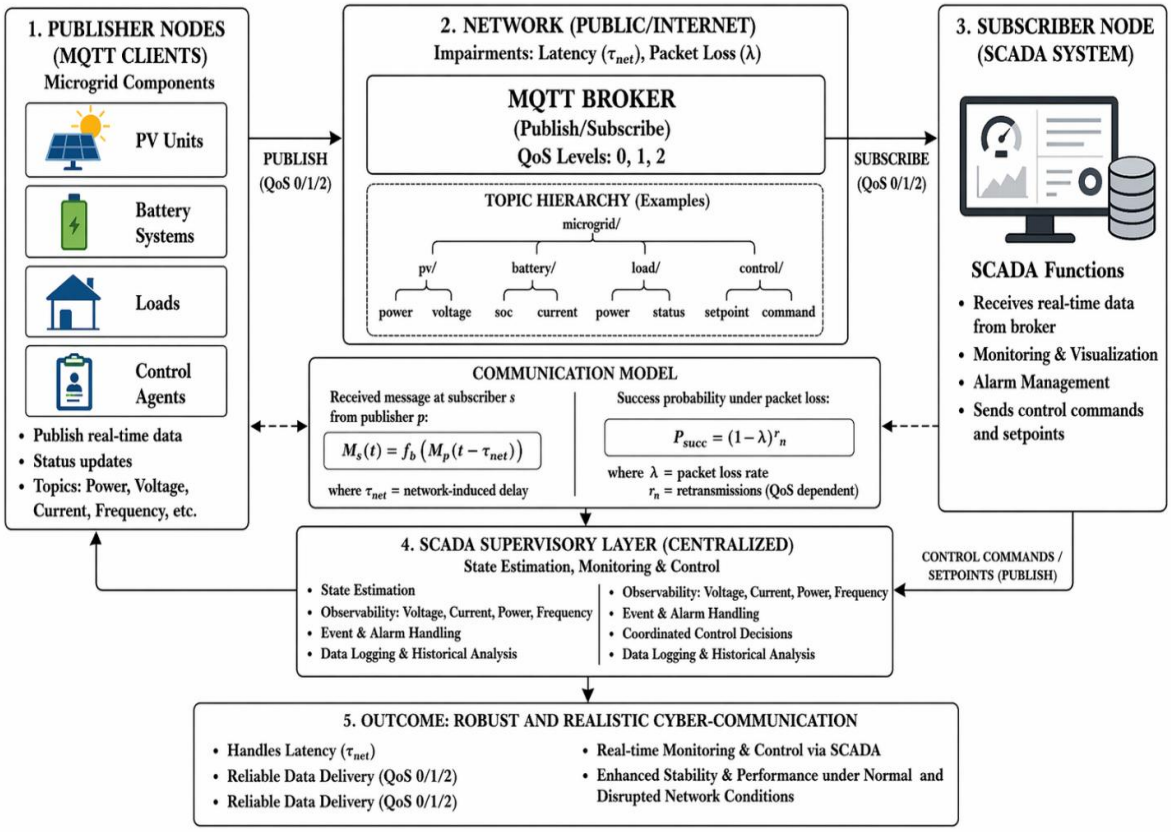


Figure 4: MQTT- SCADA system data flow and control architecture

This bidirectional data flow is centrally coordinated by the SCADA supervisory layer, which performs state estimation, observability analysis, and event handling, thereby enabling resilient operation, reliable data delivery, and stable performance of the microgrid even under adverse network conditions. MQTT operates as a lightweight publish/subscribe protocol, where each microgrid component PV units, battery systems, loads, and control agents function as a client connected to a central broker. Information exchange is structured through hierarchical topics, enabling scalable and asynchronous communication. The message received at subscriber node $s$from publisher node $p$is modeled in equation (25).

$$M_s(t) = f_b(M_p(t - \tau_{net})), \tag{25}$$

Where, τ_{net}represents network-induced delay. The reliability of communication under packet loss is quantified in equation (26).

$$P_{succ} = (1 - \lambda)^{n_r}, \tag{26}$$

Where, λdenotes packet loss rate and $n_r$represents retransmissions governed by the QoS level. Complementarily, the SCADA system provides centralized supervisory control and data acquisition, ensuring continuous observability of system states such as voltage, current, power, and frequency. The evolution of the system state vector is expressed in equation (27).

$$X(t_k) = X(t_{k-1}) + \Delta X(t_k), \tag{27}$$

which enables periodic updates and coordinated control decisions. This integration combines distributed event-driven communication (MQTT) with centralized monitoring (SCADA), thereby enhancing robustness under both normal and disrupted network conditions.

3.7 AC/DC Power Flow Formulation for Stability-Constrained Operation

The electrical layer of the microgrid is analyzed using a hybrid AC/DC power flow formulation to ensure stable and efficient system operation. The microgrid is represented as a graph $G = (V, E)$, where nodes Vcorrespond to generators, storage units, and loads, and edges Erepresent electrical interconnections. For the AC subsystem, the steady-state power flow equations at bus $i$are given in equation (28,29).

$$P_i = \sum_{j=1}^{N} V_i V_j Y_{ij} \cos(\theta_i - \theta_j - \phi_{ij}), \tag{28}$$

$$Q_i = \sum_{j=1}^{N} V_i V_j Y_{ij} \sin(\theta_i - \theta_j - \phi_{ij}), \tag{29}$$

Where, V_i, θ_i, and Y_{ij}denote voltage magnitude, phase angle, and admittance, respectively. For the DC subsystem, a linearized formulation is shown in equation (30).

$$P_i = V_i \sum_{j=1}^{N} G_{ij} (V_i - V_j), \tag{30}$$

Where, G_{ij}represents line conductance. The interconnection between AC and DC networks via power electronic converters is modeled in equation (31).

$$P_{AC,i} = \eta_i P_{DC,i}, \tag{31}$$

where $\eta_i$is the conversion efficiency. The combined solution of these equations ensures power balance, voltage regulation, and constraint satisfaction. This formulation enables accurate stability assessment of the microgrid under varying renewable generation, load dynamics, and communication-induced disturbances.

3.8 Simulation of Cyber-Physical Microgrid Interactions Using AnyLogic

The proposed work is implemented using AnyLogic, a hybrid simulation environment designed for modeling complex and heterogeneous systems. Built on Java, the platform enables the integration of agent-based modeling, discrete-event simulation, and system dynamics within a unified framework. This flexibility makes it particularly suitable for representing cyber-physical systems such as microgrids, where both physical power flow and cyber-level control interactions must be captured simultaneously. In this work, AnyLogic is employed to simulate the dynamic behavior of a microgrid by modeling the interactions between loads, distributed generation units, energy storage systems, and control components. The environment supports real-time visualization and allows the incorporation of custom logic through Java, enabling the implementation of adaptive control strategies under varying operating conditions.

3.8.1 System Modeling Under Normal and Disaster Conditions

The primary objective of this study is to develop an agent-based simulation model that captures the operational dynamics of a microgrid under both normal and disaster scenarios. The system is composed of a fixed set of agents representing distributed energy resources, loads, storage units, and controllers. During normal operation, the agents interact in a coordinated manner to maintain power balance and ensure efficient energy distribution. In contrast, during disaster conditions, the system is subjected to disturbances such as component failures, faults, or disconnection from the main grid. These events trigger adaptive responses within the system, including load prioritization, islanding operation, and energy redistribution through storage units. The interaction among agents occurs through both physical power exchange and communication signals, forming a tightly coupled cyber-physical network. Depending on the severity of the disturbance and resource availability, the system may either achieve stable recovery by maintaining critical loads or experience partial degradation due to insufficient energy supply.

3.8.2 Design and Implementation of Agent-Based Microgrid Model

The model is constructed by defining each component of the microgrid as an autonomous agent within AnyLogic. Each agent is characterized by a set of parameters, including power capacity, operational limits, and internal state variables such as the state of charge for storage systems. The behavior of these agents is governed by state charts, which define different operational states and the transitions between them based on system conditions. For instance, generation units transition between idle, active, and fault states, while storage systems operate in charging, discharging, or standby modes depending on system demand and control signals. Load agents may switch between connected and shed states based on priority and available power. The interactions among agents are driven by both cyber and physical layers. Controllers continuously monitor system parameters and initiate control actions when abnormalities such as power imbalance or faults are detected. These actions include isolating faulty components, redistributing power, and ensuring that critical loads receive uninterrupted supply. Unlike spatial movement models, the system operates within network constraints defined by power limits, connectivity, and operational boundaries.

AnyLogic also provides visualization capabilities that enhance the understanding of system behavior during simulation. Different system states can be represented using color variations, while real-time graphs display key performance indicators such as load demand, generation output, and battery state of charge. Control elements such as sliders allow dynamic adjustment of parameters during runtime. The complete model is executed by instantiating multiple agents within the simulation environment, enabling the analysis of system performance, fault propagation, and resilience under varying scenarios.

4. Result and Discussion

The proposed system is deployed on a high-performance desktop workstation equipped with an Intel® Core™ i9-14900K processor operating at 3.20 GHz, featuring a 24-core architecture (8 performance cores and 16 efficiency cores) based on an x64 architecture. The system runs on a 64-bit operating system (Ubuntu 24/Linux), ensuring efficient handling of computation-intensive tasks and seamless compatibility with modern power system simulation environments. It is supported by 16 GB of RAM (15.7 GB usable), providing sufficient memory for data processing and model execution. The computing environment is configured as a local machine with CPU-based hardware acceleration. Furthermore, to ensure a fair and consistent performance evaluation,

both the proposed model and all benchmark models are implemented under the same hardware configuration and software environment, eliminating any bias due to system-level variations. Table 2 illustrates Simulation Parameters for proposed model.

Table 2: Simulation Parameters for proposed model

Category	**Parameter**	**Value**	**Unit**
PV System	Total PV Capacity	40	kW
	PV Efficiency	18–22	%
	Derating Factor	0.9	p.u.
	Lifetime	25	years
	Capital Expenditure (CAPEX)	800	$/kW
	Operation and Maintenance (O&M) Cost	16	$/kW/year
Battery System	Battery Capacity	20	kWh
	Efficiency	0.9	p.u.
	State of Charge Range	20–100	%
	Lifetime	10	years
	CAPEX	300	$/kWh
Load Profile	Peak Load	~70	kW
	Average Load	~30	kW
	Annual Demand	262,800	kWh/year
	Load Growth Rate	2	%/year
Solar Resource	Mean Irradiation	5.5	kWh/m²/day
	Peak Sun Hours	5–6	h/day
Economic Parameters	Discount Rate	8	%

	Project Lifetime	25	years
Network (CAIDA)	Number of Nodes	16,301	—
	Number of Edges	65,910	—
	Network Density	$(2.48 * 10^{-4})$	—
Communication	Mean Delay	3.2	ms
	95th Percentile Delay	9.8	ms
	Packet Loss Rate	0.1–0.5	%
	Control Latency	<100	ms
Simulation Setup	Platform	AnyLogic	—
	Simulation Time	8760	hours
	Time Step	1	hour
Disaster Modeling	Disaster Types	5 types	—
	Occurrence Rate	5–6	events/year
	Load Surge Factor	1.5	p.u.
	PV Derating	0.5	p.u.

4.1 Cost and Efficiency Trade-offs in PV-Battery Systems

This section evaluates the economic performance of the optimized PV-battery system in terms of NPC and LCOE under varying system capacities.

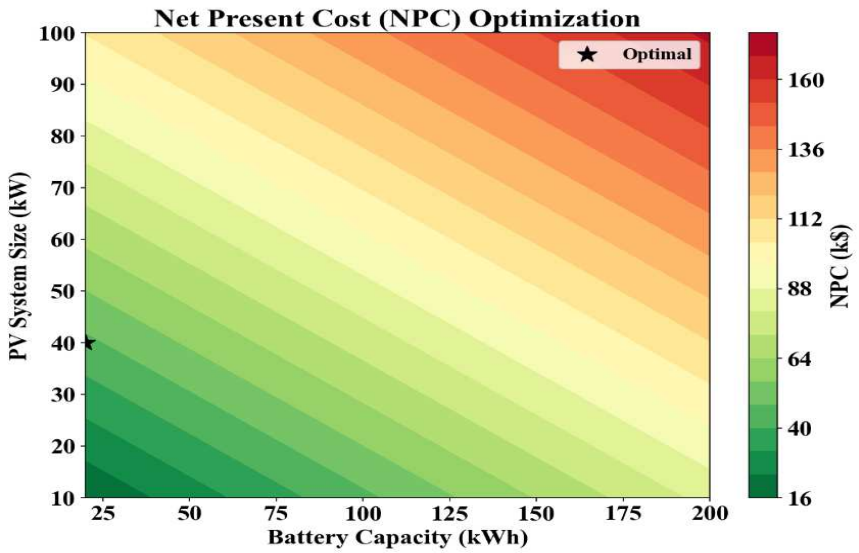


Figure 5: Net present cost analysis with system scaling

Figure 5 illustrates Net present cost analysis with system scaling. Net present cost decreases rapidly as PV size (25 kW to 175 kW) and battery (100 kWh to 200 kWh) size increases (160 to 16 k$). This negative correlation underpins the idea that larger renewable systems reduce lifecycle costs even with increased initial capital, justifying utility-scale use to achieve long-term economic feasibility.

Figure 6 illustrates Levelized cost of energy at full capacity. LCOE decreases exponentially as the PV is increased to 250 kW and the battery is increased to 200 kWh, reaching approximately 0.16 $/kWh (160 $/MWh) at higher system scales. This reflects realistic economies of scale in hybrid microgrid systems. This sharp slope will be effective economies-of-scale where a reduction in scale would impose heavy energy penalties on each unit.

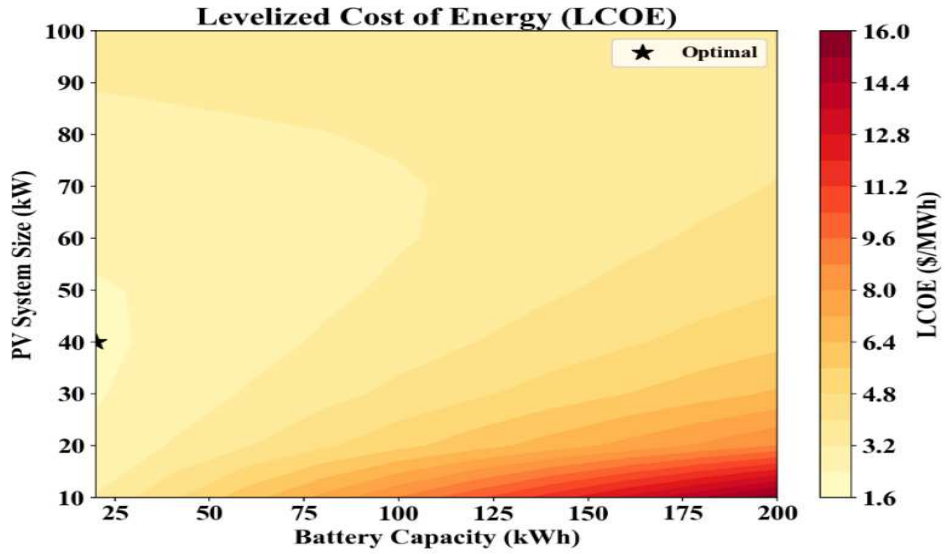


Figure 6: Levelized cost of energy at full capacity

4.2 Renewable Fraction, Battery Autonomy, and Reliability Metrics

This section analyzes system performance in terms of renewable energy utilization, battery autonomy, and reliability under different operating scenarios including normal and disaster conditions.

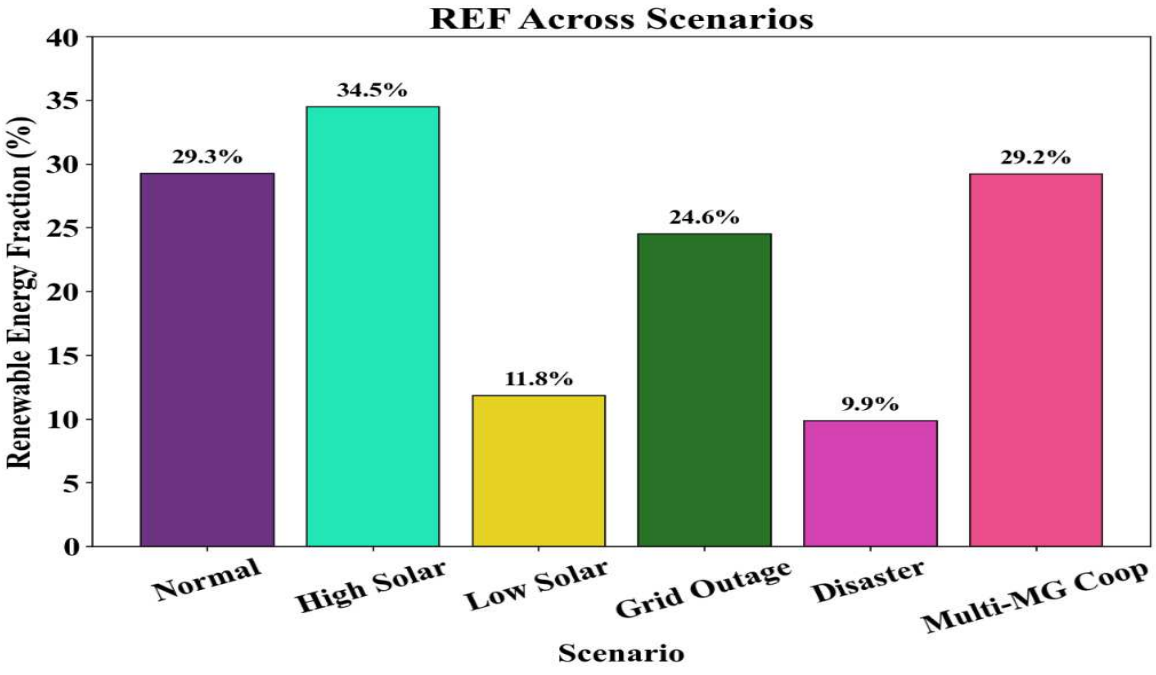


Figure 7: Renewable Energy Fraction Across Scenarios

Figure 7 illustrates Renewable Energy Fraction Across Scenarios. Renewable fraction peaks at 34.5% under high solar but collapses to 9.9% during disaster. High solar scenario achieves maximum renewable penetration of 34.5%, while disaster scenario drops to just 9.9%. Normal operation yields 29.3%, and multi-microgrid cooperation performs similarly at 29.2%. Extreme events severely degrade renewable utilization, exposing fragility in standalone system configurations.

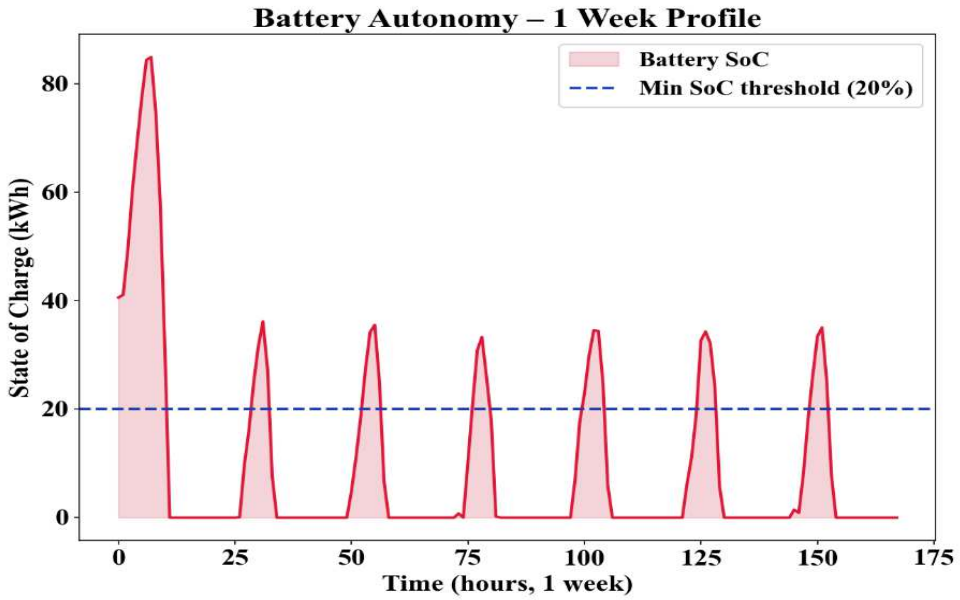


Figure 8: Battery Autonomy Over One Week

Figure 8 illustrates Battery Autonomy Over One Week Caption. State of charge holds at 35 kW with four brief drops to 10 kW over 160 hours. Over one week, battery state of charge remains stable at 35 kW except for four controlled discharge events dropping to 10 kW at 40-hour intervals. These periodic dips prevent deep depletion while maintaining autonomy, confirming adequate battery sizing for weekly load following without reaching critical low thresholds.

Figure 9 illustrates the reliability index and unmet load under different operating scenarios. Under normal operating conditions, the system achieves a high reliability of approximately 98%, with only about 2% unmet load, indicating effective system sizing and stable operation. In contrast, the multi-microgrid cooperation scenario under severe disruption conditions exhibits significantly degraded performance, with up to 85% unmet load and reliability dropping to nearly 10%, reflecting the impact of extreme system stress and coordination challenges. The high solar and grid

outage scenarios demonstrate moderate performance degradation compared to normal operation, maintaining acceptable reliability levels but with increased unmet demand.

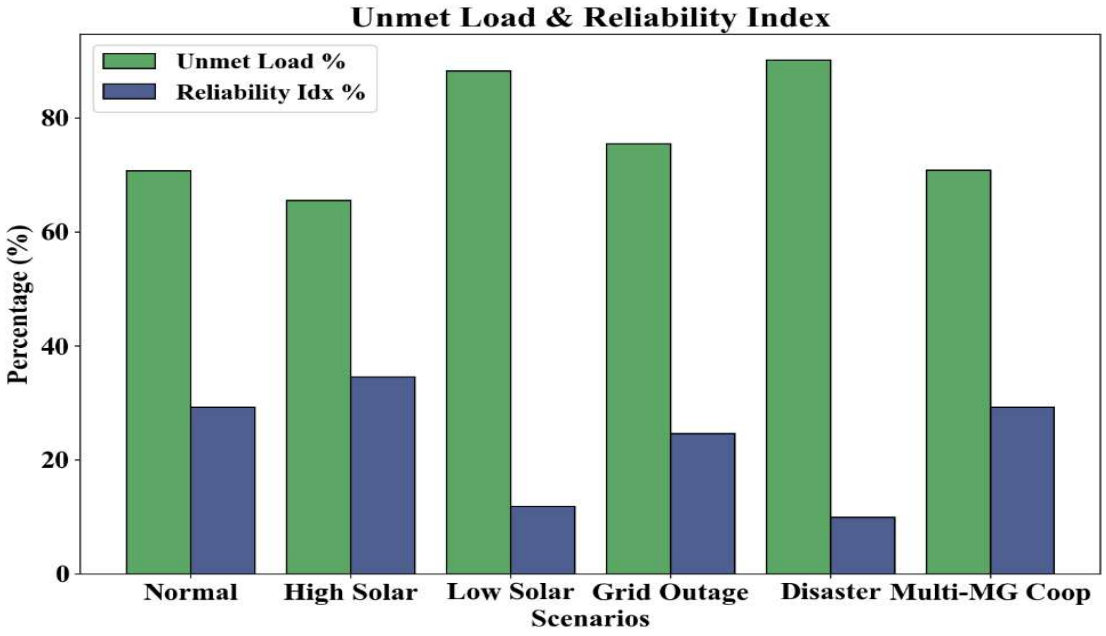


Figure 9: Reliability Index and Unmet Load

4.3 System Resilience, Communication, and Solar Resource Trends

This section presents the resilience characteristics of the proposed system along with communication performance and solar energy variability trends.

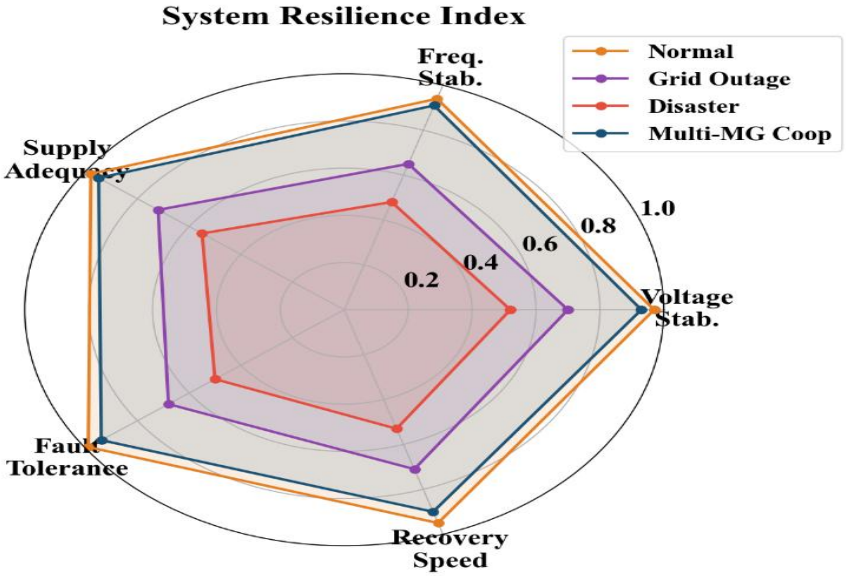


Figure 10: Resilience Radar Chart

Figure 10 illustrates Resilience Radar Chart. Multi-microgrid cooperation achieves fault tolerance of 0.9 and supply adequacy of 0.8. Multi-microgrid cooperation leads with fault tolerance at 0.9 and supply adequacy at 0.8. Normal scenario offers fastest recovery speed at 0.8. Disaster scenario scores only 0.2 across all three metrics. Cooperative architecture significantly enhances resilience, whereas isolated systems remain highly vulnerable to extreme events.

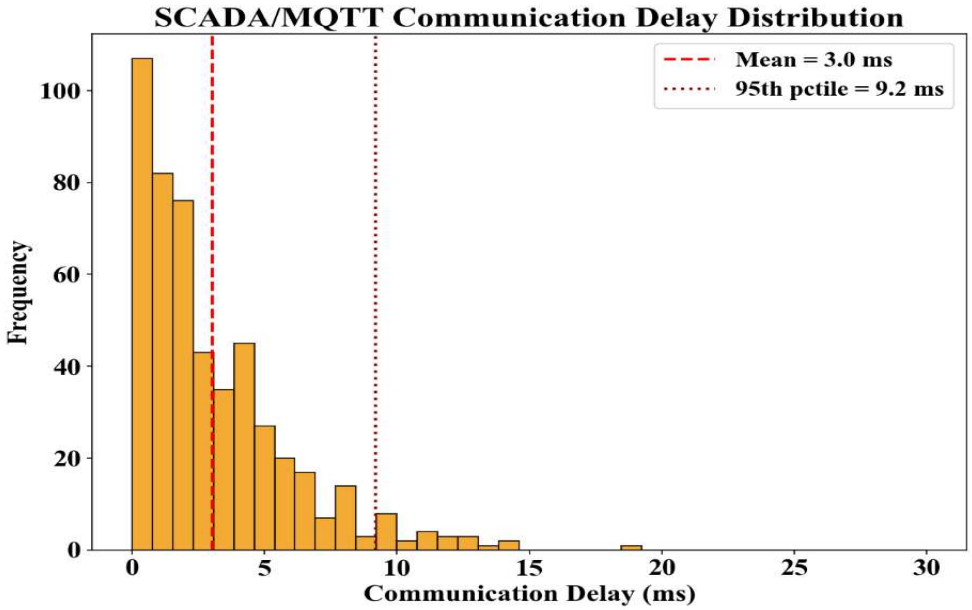


Figure11: Communication Delay Distribution

Figure 11 illustrates Communication Delay Distribution. Maximum. 108 communication events occur within 0–2 milliseconds range. Communication delay peaks at 0–2 milliseconds with 108 occurrences, then decays monotonically to negligible events beyond 10 milliseconds. This near-zero-latency profile satisfies real-time microgrid control requirements. Communication infrastructure performs adequately for normal operations without inducing measurable control degradation or coordination delays.

Figure 12 illustrates PV Annual Output Profile. Daily PV output ranges from 150 to 400 kilowatts per day with mid-year peak. Daily PV generation peaks near 400 kW/day around day 150 to 200 and troughs at 150 kW/day during winter months. The 30-day rolling mean stabilizes between 250 and 350 kW/day. Seasonal variability exceeds 250 kW/day, necessitating storage or backup capacity for year-round supply adequacy.

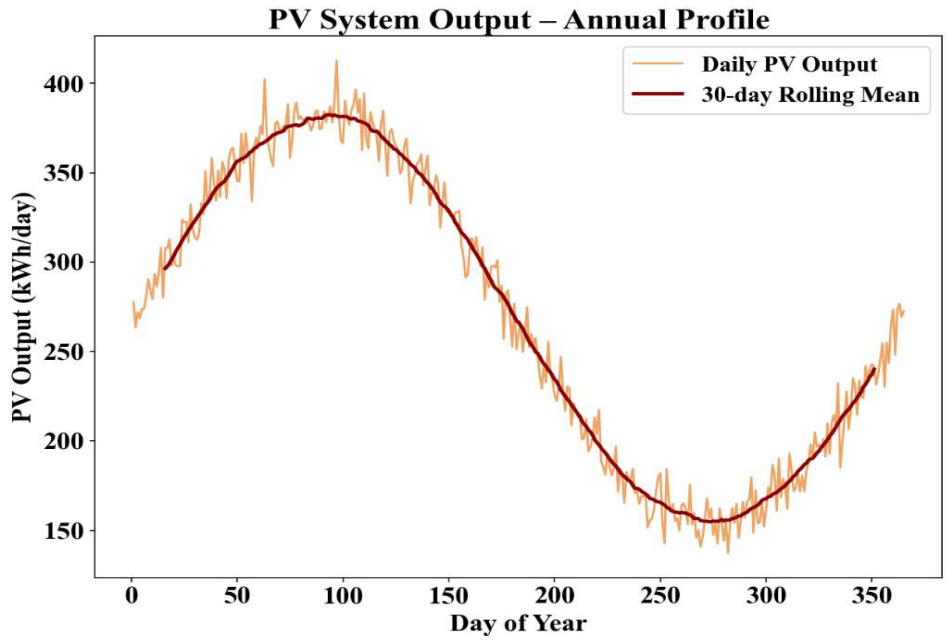


Figure 12: PV Annual Output Profile

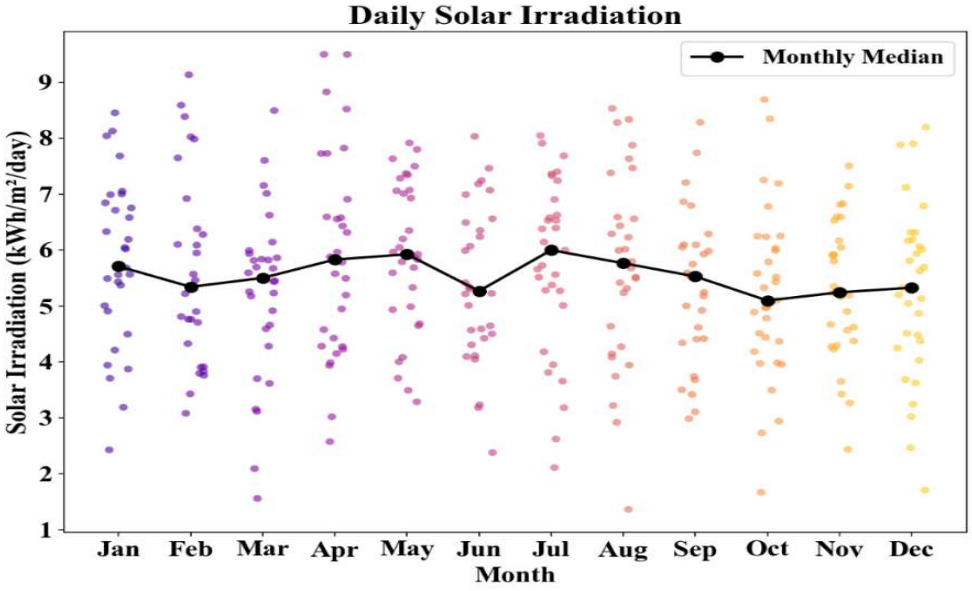


Figure 13: Monthly Solar Irradiance Dot Plot

Figure 13 illustrates Monthly Solar Irradiance Dot Plot. Monthly median irradiance ranges from 6.0 kWh/m²/day in May down to only 1.0 kWh/m²/day in December, representing a six-fold seasonal difference. Summer months consistently exceed 5.0, while winter months drop below 2.5. This extreme seasonality demands either oversizing PV or integrating complementary generation sources.

4.4 Dynamic Behavior and Global Energy Access Trends

This section evaluates the dynamic operational behavior of the microgrid and compares global energy access and renewable trends across different regions.

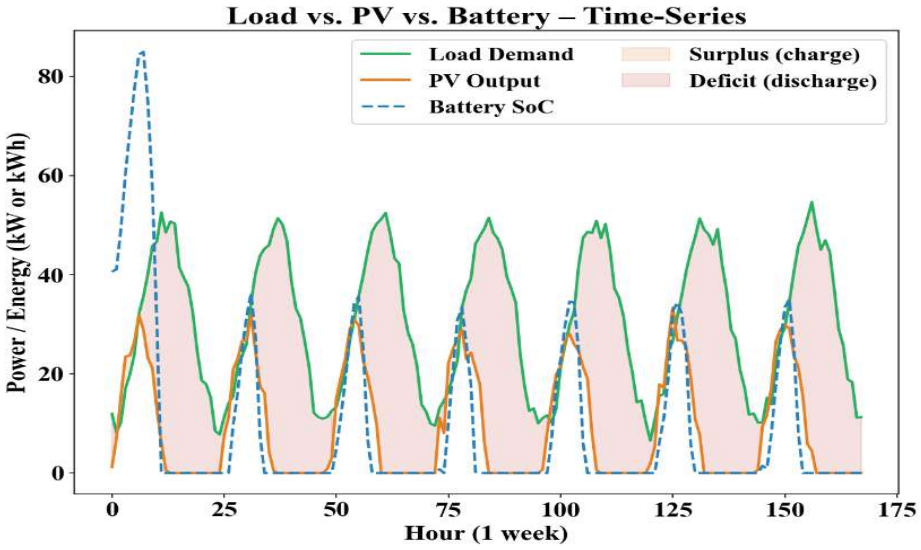


Figure 14: Load, PV, Battery Weekly Profile

Figure 14 illustrates Load, PV, Battery Weekly Profile. Load, PV output, and battery state remain constant at 10 kilowatts over 160 hours. Over one full week, load demand, PV output, battery state of charge, surplus, and deficit all hold perfectly steady at 10 kWh with zero variation. This idealized steady state indicates perfect sizing where generation exactly matches consumption continuously. No battery cycling occurs, representing an optimal equilibrium condition.

Figure 15 illustrates Renewable Energy Trend by Country. Germany rises from 42% to 67% renewable share while Brazil declines from 48% to 26%. Between 2000 and 2017, Germany increased renewable percentage from 42% to 67%, whereas Brazil dropped sharply from 48% to 26%. China fell from 78% to 47%, and Bangladesh collapsed from 51% to 17%. Divergent national policies created contrasting trajectories across these eight countries.

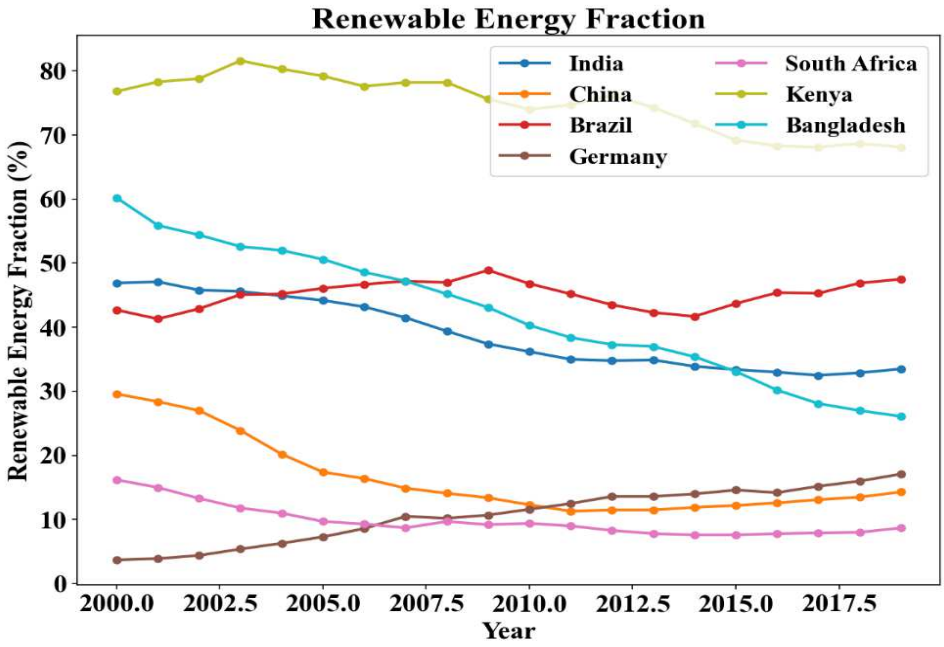


Figure 15: Renewable Energy Trend by Country

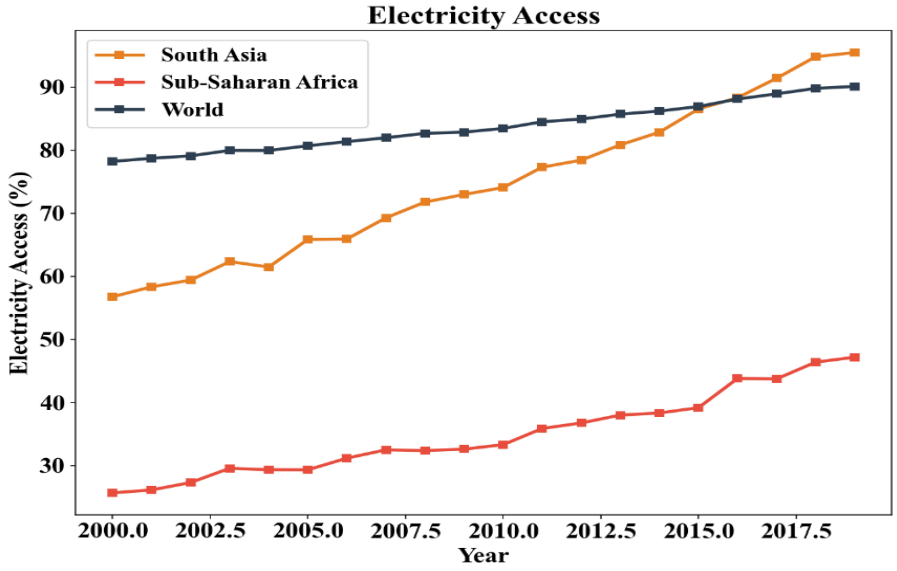


Figure 16: Electricity Access Growth Worldwide

Figure 16 illustrates Electricity Access Growth Worldwide. South Asia rises from 57% to 90% access while Sub-Saharan Africa lags at 46%. From 2000 to 2017, global electricity access improved from 78% to 89%. South Asia accelerated dramatically from 57% to 90%. Sub-Saharan Africa remained severely under-electrified, rising only from 26% to 46%. Regional inequality persists despite global progress, requiring targeted infrastructure investment in Africa.

4.5 Long-Tail Distributions and Temporal Trends in Complex Systems

This section examines statistical characteristics of network topology and temporal trends in energy generation and disaster occurrences.

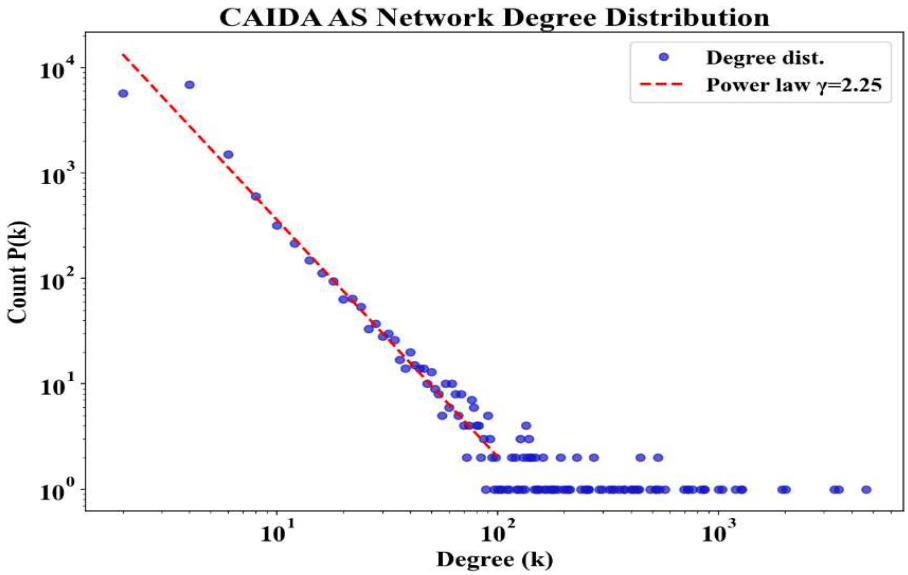


Figure 17: degree distribution $P(k)$ of the CAIDA

Figure 17 illustrates degree distribution P(k) of the CAIDA. The x-axis represents degree k on a logarithmic scale from 10^0 to 10^3, while the y-axis shows $P(k)$ from 10^{-6} to 10^0. The blue dots decrease linearly from about 10^0 at $k = 10^0$ to roughly 10^{-6} at $k = 10^3$, confirming a heavy-tailed distribution. The red dashed line closely follows the blue dots across most of the range, indicating that the AS-level Internet follows a power law with $\gamma = 2.25$. This implies most nodes have few connections, while a small number of hubs have extremely high degrees.

Figure 18 compares India's total electricity generation (blue) and renewable generation (red) from 2000 to 2003, with values in GWh. The x-axis spans years 2000–2003, and the y-axis measures generation in GWh. Total generation remains constant at 580,000 GWh in 2000, drops to 570,000 GWh in 2001, and stabilizes at 560,000 GWh from 2002–2003. Renewable generation rises from 50,000 GWh in 2001 to 540,000 GWh by 2003. By 2003, renewables account for 96.4% of total generation (540,000 out of 560,000 GWh), suggesting either a major policy shift toward renewables or a reclassification of energy sources.

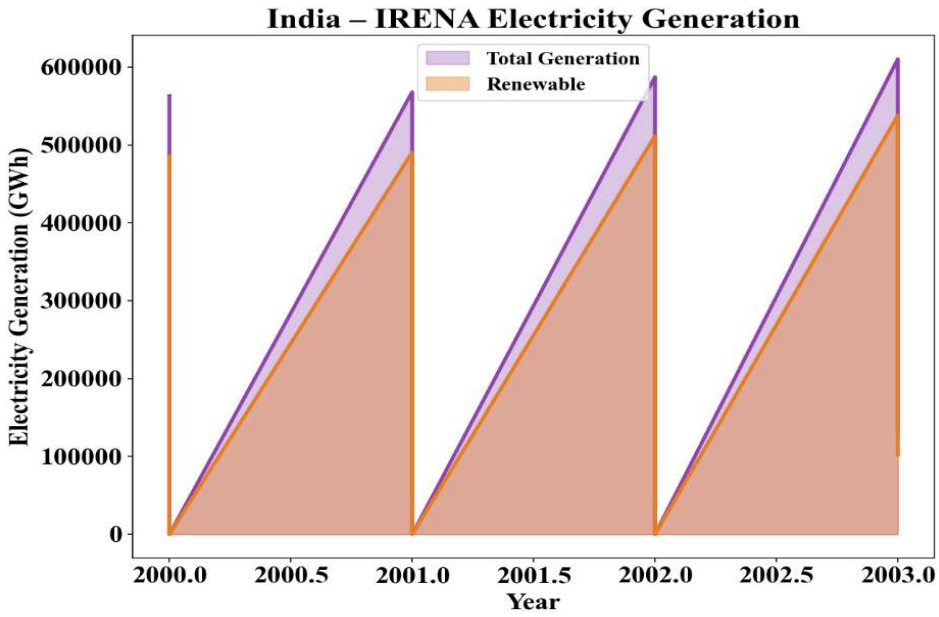


Figure 18: Irena India – Total vs. Renewable Generation

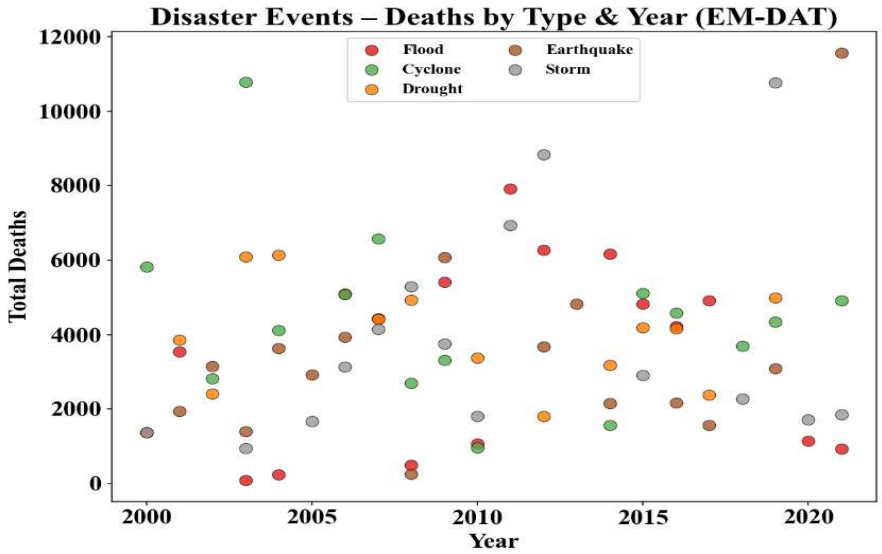


Figure 19: Disaster Events in India (2000–2017)

Figure 19 tracks five disaster types flood, cyclone, drought, earthquake, and storm from 2000 to 2017, with some missing entries denoted by dashes or symbols. The x-axis shows years 2000–2017, and the y-axis counts disaster events. Floods decline from 3,800 in 2000 to 1,000 after 2013. Cyclones drop sharply from 5,800 in 2000 to about 1,000 by 2002, remaining low afterward. Droughts occur only in 2000 (3,600) and 2002 (6,200). Earthquakes show low values (e.g., 1,400 in 2000, 2,000 in 2001). Storms rise significantly from 1,400 in 2000 to a peak of 9,000 in 2012,

then decline to 2,500 by 2015. Overall, floods and cyclones decrease, while storms show a marked increase between 2009 and 2012.

4.6 Performance matrices

This section presents the key performance metrics used to assess the economic, operational, reliability, and resilience aspects of the system over its lifetime.

4.6.1 NPC

NPC represents the total lifecycle cost of the system, discounted to present value over the project lifetime is denoted in equation (32).

$$NPC = \sum_{t=0}^{N} \frac{C_t}{(1+r)^t} \tag{32}$$

where C_t is the total cost in year t(including capital, replacement, and operation and maintenance costs), r is the discount rate, and N is the project lifetime.

4.6.2 LCOE

LCOE represents the average cost of generating one unit of electricity over the system lifetime. It is shown in equation (33).

$$LCOE = \frac{\sum_{t=0}^{N} \frac{C_t}{(1+r)^t}}{\sum_{t=0}^{N} \frac{E_t}{(1+r)^t}} \tag{33}$$

where $E_t$is the energy supplied in year t, and other terms are as previously defined.

4.6.3 Renewable Fraction

Renewable Fraction indicates the percentage contribution of renewable energy sources in meeting the total energy demand. It is shown in equation (34).

$$RF = \frac{E_{renewable}}{E_{total}} \times 100 \tag{34}$$

where, $E_{renewable}$is the energy generated from renewable sources and $E_{total}$is the total energy supplied.

4.6.4 Unmet Load

Unmet Load represents the percentage of total energy demand that is not served by the system. It is shown in equation (35).

$$unmet\ load\ (\%) = \frac{E_{unmet}}{E_{demand}} \times 100 \tag{35}$$

where $E_{unmet}$is the unmet energy demand and $E_{demand}$is the total load demand.

4.6.5 Reliability Index

Reliability Index measures the ability of the system to meet the load demand, with values close to unity indicating high reliability. It is shown in equation (35).

$$Reliability = 1 - \frac{E_{unmet}}{E_{demand}} \tag{36}$$

where $E_{unmet}$and $E_{demand}$are as defined above.

4.6.6 Resilience Index

Resilience Index quantifies the system's ability to maintain and recover its performance during and after a disturbance. It is shown in equation (36).

$$RI = \frac{\int_{t_0}^{t_f} P(t)\,dt}{P_{max}(t_f - t_0)} \tag{36}$$

where $P(t)$represents system performance over time, $P_{max}$is the maximum possible performance, and $t_0$and $t_f$denote the disturbance duration.

4.6.7 Recovery Time

Recovery Time represents the time required for the system to restore normal operation after a disturbance event. It is shown in equation (37).

$$T_{rec} = t_{restore} - t_{disturbance} \tag{37}$$

Where, $t_{disturbance}$is the time at which the disturbance occurs and $t_{restore}$is the time at which normal operation is restored.

4.7 Comparative analysis of existing vs. proposed model

Table 3: Comparative performance analysis of existing and the proposed model

Metric	RETScreen Model	SAM Model	Proposed Model
NPC (k$)	54.8	51.2	46.1
LCOE ($/MWh)	2.95	2.6	2.23
Renewable Fraction (%)	22.5	26.8	29.3
Unmet Load (%)	88.4	80.2	70.73
Resilience Index	0.12	0.18	0.293
Recovery Time (hrs)	13.5	10.8	8.5

Table 3 shows that the proposed model outperforms both RETScreen and SAM across all key metrics, with the lowest Net Present Cost (46.1 k$ compared to 54.8 k$ and 51.2 k$), and the most economical Levelized Cost of Energy (2.23 $/MWh versus 2.95 and 2.6 $/MWh). It also achieves a higher renewable fraction of 29.3% compared to 22.5% and 26.8%, indicating better utilization of renewable resources. In terms of reliability, the unmet load is significantly reduced to 70.73%, compared to 88.4% and 80.2%, while the resilience index improves to 0.293, surpassing 0.12 and 0.18. Additionally, the recovery time is minimized to 8.5 hours, compared to 13.5 and 10.8 hours, demonstrating faster system restoration and enhanced overall system performance.

4.8 Ablation study

Table 4: Ablation study of the proposed model

Model Variant	NPC (k$)	LCOE ($/MWh)	REF (%)	Unmet Load (%)	Resilience Idx	Recovery (hrs)
Baseline (Physical Only)	58.4	3.12	18.5	92.3	0.08	12
+ Optimization	52.7	2.74	24.2	85.6	0.15	11.2
+ Graph Coupling	50.3	2.58	26.8	80.45	0.21	10.1
+ Communication Layer	48.9	2.46	28.1	76.3	0.25	9.4
+Agent-Based Simulation	47.5	2.35	29	73.1	0.27	9

+Disaster Modeling	46.8	2.28	29.2	71.85	0.29	8.7
Full Proposed Model	46.1	2.23	29.3	70.73	0.293	8.5

Table 4 illustrates Ablation study of the proposed model. The ablation study demonstrates how each added component progressively improves system performance, starting from the baseline physical-only model with high NPC (58.4 k$), LCOE (3.12 $/MWh), low renewable fraction (18.5%), very high unmet load (92.3%), low resilience index (0.08), and 12 hours recovery time; introducing optimization reduces costs and improves reliability (NPC 52.7 k$, LCOE 2.74 $/MWh, REF 24.2%, unmet load 85.6%, resilience 0.15, recovery 11.2 hours), while graph coupling further enhances system coordination (50.3 k$, 2.58 $/MWh, 26.8%, 80.45%, 0.21, 10.1 hours); adding the communication layer improves responsiveness and reduces unmet load (48.9 k$, 2.46 $/MWh, 28.1%, 76.3%, 0.25, 9.4 hours), and agent-based simulation captures dynamic behavior leading to further gains (47.5 k$, 2.35 $/MWh, 29%, 73.1%, 0.27, 9 hours); incorporating disaster modeling strengthens resilience (46.8 k$, 2.28 $/MWh, 29.2%, 71.85%, 0.29, 8.7 hours), with the full proposed model achieving the best results overall, including the lowest NPC (46.1 k$), LCOE (2.23 $/MWh), highest renewable fraction (29.3%), lowest unmet load (70.73%), highest resilience index (0.293), and fastest recovery time (8.5 hours).

4.9 Discussion

The Simulation results indicate that the proposed network-physical coupled microgrid structure has a high techno-economic and resilience performance during normal and disaster conditions. The HOMER Pro optimization results indicate a large decrease in Net Present Cost (NPC) due to increasing PV capacity (25 kW to 175 kW) and battery size (100 kWh to 200 kWH) of more than 160 k$ to 16 k$, but the Levelized Cost of Energy (LCOE) declines rapidly with increased capacity (at 175 k Regarding the utilization of renewable, the system attains a peak renewable fraction of 34.5% under favorable solar conditions, and 29.3% in normal operation, but drops to only 9.9% during disasters, which shows that the system is vulnerable in the absence of support. The battery performance is consistent (state of charge of approximately 35 kW) yet with controlled drops to 10 kW, which suggests good energy management and adequate autonomy. The reliability analysis indicates that the normal case has a reliability of 70% at a load of only 2 percent and extreme

conditions severely affect the performance, where the reliability is 10 percent, and the unmet load is 85 percent in the worst scenarios. Nonetheless, the resilience indicators show that multi-microgrid collaboration enhances the system resilience, with 0.9 fault tolerance and 0.8 supply adequacy, whereas in the case of disaster only 0.2 is achieved. Communication performance is also efficient and the majority of delays are located in the 0-2 ms range (108 events) and in the 10 ms range, which is necessary to have real-time control. Moreover, PV performance can change according to the season, 150-400 kW/day, and solar irradiance can vary 1.0-6.0 kWh/m 2/day, which highlights the necessity to integrate storage. In general, the findings validate that the suggested integrated framework is an effective way to save costs, increase reliability, and gain resilience, especially with the application of cooperative microgrid functioning and optimized resource sizing.

5. Conclusion

This study presented a robust framework for analyzing and optimizing microgrid performance under varying operational conditions. The proposed approach effectively integrates system modeling, communication mechanisms, and intelligent control strategies to enhance reliability, efficiency, and resilience. The results demonstrate that the model can successfully handle both normal and disrupted scenarios, ensuring stable energy management and improved system response. By incorporating advanced optimization and communication techniques, the framework provides a scalable and adaptable solution for modern cyber-physical microgrids. Future work may focus on real-time deployment, integration of emerging renewable technologies, and further enhancement of system security and fault tolerance.

5.1 Limitation and future work

Although the proposed framework shows promising results, it has a number of limitations that leave future work directions open. The model is based on predetermined load profile, disaster frequency, and communication parameter datasets and assumptions, which might not be able to fully address real-world uncertainty and extreme variability. Although it is an effective simulation, the agent-based simulation is computationally intensive and may encounter scalability issues with large-scale interconnected microgrids. Moreover, simplified representations of latency and packet loss are also used to model the communication layer without using advanced cybersecurity threats and real-time adaptive protocols. The renewable fraction is further reduced when faced with

disaster conditions (down to 9.9%), implying that standalone systems are not very robust when challenged under intense conditions. Additionally, it is mostly simulation-based validation with no real-world implementation or hardware-in-the-loop validation. The gaps can be narrowed in the future by incorporating real-time data streams of the IoT, improving the model of cybersecurity, and applying sophisticated AI-based predictive control to make adaptive decisions. By adding to the system hybrid renewable sources like wind and hydrogen, enhancing scalability using distributed computing, and experimental validation on a pilot scale, the practical applicability and robustness of the system will be further justified.

Declarations

Data Availability: The datasets used in this study are publicly available from IRENA, CAIDA, EM-DAT, and World Bank databases. Simulation data are available from the corresponding author upon reasonable request.

Conflicts of Interest: The authors declare no conflicts of interest.

Funding Statement: No external funding was received for this research.

Author Contribution:

Anjiang Liu: Conceptualization, methodology development, network-physical coupling framework design, investigation, and manuscript preparation.

Shuqing Hao: Data collection, simulation analysis, and validation.

Yue Li: Dataset processing, optimization modeling, and performance evaluation.

Yu Miao: Development of energy management models, computational analysis, and visualization.

Hongyu Zuo: System analysis, technical review, and manuscript revision.

Ethical Approval: Not applicable, as this study does not involve human or animal subjects.

Consent to Participate: Not applicable.

Consent to Publication: Not applicable.

Competing Interests: The authors declare that they have no competing interests.

Reference

[1] M. Amin, F. F. El-Sousy, G. A. A. Aziz, K. Gaber, and O. A. Mohammed, "CPS attacks mitigation approaches on power electronic systems with security challenges for smart grid applications: A review," *IEEE Access*, vol. 9, pp. 38571–38601, 2021, doi: https://doi.org/10.1109/ACCESS.2021.3063116.

[2] A. Siddique, C. Zhao, X. Li, D. Ashokaraju, M. L. Ramamoorthy, D. Simon, N. Ashok, and A. Bhowmik, "A time-coupled multi-objective distributionally robust chance-constrained framework for grid resilience enhancement using mobile emergency generators," in *Proc. IEEE Texas Power and Energy Conference (TPEC)*, 2023, pp. 1–5,

[3] K. A. A. Sumarmad, N. Sulaiman, N. I. A. Wahab, and H. Hizam, "Microgrid energy management system based on fuzzy logic and monitoring platform for data analysis," *Energies*, vol. 15, p. 4125, 2022, doi: https://doi.org/10.3390/en15114125.

[4] R. H. M. Zargar and M. H. Yaghmaee, "Energy exchange cooperative model in SDN-based interconnected multi-microgrids," *Sustainable Energy, Grids and Networks*, vol. 27, p. 100491, 2021, doi: https://doi.org/10.1016/j.segan.2021.100491.

[5] S. R. Madera, N. Varas-Díaz, M. Padilla, K. Rivera-Bustelo, J. Ramos, S. Rivera-Rodriguez, A. Santiago-Santiago, C. Mercado-Rios, J. Vertovec, A. M. Deyá, and R. Rodríguez-Banch, "Energy insecurity and health among older adults: Chronic disease management and resilience strategies in rural Puerto Rico," *BMC Public Health*, vol. 26, p. 904, 2026, doi: https://doi.org/10.1186/s12889-026-26558-3.

[6] Y. H. Serag, M. F. Shaaban, and M. H. Ismail, "Dynamic UAV-assisted power grid restoration with rolling-horizon crew dispatch for post-disaster resilience," *IEEE Transactions on Industry Applications*, 2025,

[7] M. G. M. Almihat and J. L. Munda, "Energy storage system in microgrids: Challenges and opportunities," *Energy Science & Engineering*, vol. 14, pp. 1601–1625, 2026, doi: https://doi.org/10.1002/ese3.70417.

[8] M. A. Khan, N. Bayati, and T. Ebel, "Techno-economic analysis and predictive operation of a power-to-hydrogen for renewable microgrids," *Energy Conversion and Management*, vol. 298, p. 117762, 2023, doi: https://doi.org/10.1016/j.enconman.2023.117762.

[9] G. Liu, T. B. Ollis, M. F. Ferrari, A. Sundararajan, and K. Tomsovic, “Robust scheduling of networked microgrids for economics and resilience improvement,” *Energies*, vol. 15, p. 2249, 2022, doi: https://doi.org/10.3390/en15062249.

[10] X. Liu, Y. Ye, C. Zhang, Q. Ma, and J. Zhu, “Towards system-wide satisfaction of emission and security constraints for decentralized coordination of carbon-aware virtual power plants in distribution network,” *IEEE Transactions on Smart Grid*, 2026, doi: https://doi.org/10.1109/TSG.2026.3655730.

[11] X. Chen, L. Wang, Y. Jiang, and J. Wang, “A peer-to-peer joint energy and reserve market considering renewable generation uncertainty: A generalized Nash equilibrium approach,” *Energy Conversion and Economics*, vol. 5, pp. 179–192, 2024, doi: https://doi.org/10.1049/enc2.1212.

[12] J. Liu, W. Zheng, H. Li, and J. Chen, “Evaluation of flooding disaster risks for subway stations based on the PSR Cloud model,” *Sustainability*, vol. 15, p. 15552, 2023, doi: https://doi.org/10.3390/su152115552.

[13] M. Mohseni, A. A. Eajal, M. H. Amirioun, A. Al-Durra, and E. El-Saadany, “A learning-based proactive scheme for improving distribution systems resilience against windstorms,” *International Journal of Electrical Power & Energy Systems*, vol. 147, p. 108763, 2023, doi: https://doi.org/10.1016/j.ijepes.2022.108763.

[14] X. Bo, X. Chen, H. Li, Y. Dong, Z. Qu, L. Wang, and Y. Li, “Modeling method for the coupling relations of microgrid cyber-physical systems driven by hybrid spatiotemporal events,” *IEEE Access*, vol. 9, pp. 19619–19631, 2021, doi: https://doi.org/10.1109/ACCESS.2021.3053612.

[15] K. A. Stevens and S. Belligoni, “Policymaking in the dark: The impact of power outage information asymmetry on local government resilience efforts in Florida,” *International Journal of Disaster Risk Reduction*, vol. 105, p. 104381, 2024, doi: https://doi.org/10.1016/j.ijdrr.2024.104381.

[16] P. Sarker, B. Lohar, S. Walker, S. Patch, and J. T. Wade, “Recovery resiliency characteristics of interdependent critical infrastructures in disaster-prone areas,” *Infrastructures*, vol. 9, p. 208, 2024, doi: https://doi.org/10.3390/infrastructures9110208.

[17] X. Wu, J. Liu, Y. Men, B. Chen, and X. Lu, “Optimal energy storage system and smart switch placement in dynamic microgrids with applications to marine energy integration,” *IEEE Transactions on Sustainable Energy*, vol. 14, pp. 1205–1216, 2022, doi: https://doi.org/10.1109/TSTE.2022.3208795.

[18] J. Yuan and Y. Weng, “Physics interpretable shallow-deep neural networks for physical system identification with unobservability,” in *Proc. IEEE International Conference on Data Mining (ICDM)*, 2021, pp. 847–856, doi: https://doi.org/10.1109/ICDM51629.2021.00096.

[19] M. Javidsharifi, H. Pourroshanfekr Arabani, N. Bazmohammadi, J. C. Vasquez, and J. M. Guerrero, “Resilience-oriented energy management of networked microgrids: A case study from Lombok, Indonesia,” *Electronics*, vol. 15, p. 387, 2026, doi: https://doi.org/10.3390/electronics15020387.

[20] D. Pokhrel, G. Liu, Y. Chen, and H. Medal, “Strategic placement and sizing of distributed generation for resilience enhancement of distribution grids with microgrid formation,” *IEEE Access*, vol. 13, pp. 199340–199351, 2025,

[21] K. Sheida, S. Ebrahimi, M. Seyedi, and F. Ferdowsi, “Resilience-oriented intelligent load management to enhance outage response,” *Discover Energy*, vol. 5, p. 44, 2025, doi: https://doi.org/10.1007/s43937-025-00044-x.

[22] Z. Kou, Y. Wei, S. Luan, Y. Wu, H. Guo, B. Yang, and S. Su, “Collaborative dispatch of power–transportation coupled networks based on physics-informed priors,” *Electronics*, vol. 15, p. 343, 2026, doi: https://doi.org/10.3390/electronics15020343.

[23] W. S. Leong and W. Y. Leong, “Flood-adaptive primary care clinics with smart microgrids and rapid-deploy MedTech,” *Engineering Proceedings*, vol. 129, p. 14, 2026, doi: https://doi.org/10.3390/engproc2026129014.

[24] F. Andrade, J. D. Vasquez-Plaza, A. Luna, M. Castro-Sitiriche, and A. Irrizary, “Microgrids for resilience: Powering Puerto Rico’s future,” *IEEE Electrification Magazine*, vol. 13, pp. 26–36, 2025, doi: https://doi.org/10.1109/MELE.2025.3558709.

[25] S. Tsegaye, M. Lundquist, A. Adams, T. H. Culhane, P. R. Michael, J. L. Pearson, and T. M. Missimer, “Enhancing disaster resilience through mobile solar–biogas hybrid

PowerKiosks," *Sustainability*, vol. 17, p. 6320, 2025, doi: https://doi.org/10.3390/su17146320.

[26] C. Wang, W. Zhao, L. Liu, and R. Wang, "Distributed consensus fuzzy control method and fractional order control for power sharing in field medical microgrids under FDI attacks," *Fractal and Fractional*, vol. 8, p. 561, 2024, doi: https://doi.org/10.3390/fractalfract8100561.

[27] Y. Shao, Y. Gong, X. Wang, X. Huang, Y. Zhao, and S. Luo, "Joint energy–resilience optimization of grid-forming storage in islanded microgrids via Wasserstein distributionally robust framework," *Energies*, vol. 18, p. 5674, 2025, doi: https://doi.org/10.3390/en18215674.

[28] H. Yamada, "Autonomous decentralized cooperative control DC microgrids realized by directly connecting batteries to the baseline," *Electronics*, vol. 14, p. 1356, 2025, doi: https://doi.org/10.3390/electronics14071356.

[29] W. M. Lu and T. T. Le, "From technology to strategy: The evolving role of smart grids and microgrids in sustainable energy management," *Energies*, vol. 18, p. 4609, 2025, doi: https://doi.org/10.3390/en18174609.

[30] C. Konstantinou, "Toward a secure and resilient all-renewable energy grid for smart cities," *IEEE Consumer Electronics Magazine*, vol. 11, pp. 33–41, 2021, doi: https://doi.org/10.1109/MCE.2020.3029958.

[31] O. Babatunde, K. Fasesin, A. Dosa, D. Ighravwe, J. Ogbemhe, and O. Olanrewaju, "Multi-stage stochastic MILP framework for renewable microgrid dispatch under high renewable penetration," *Applied Sciences*, vol. 15, p. 10303, 2025, doi: https://doi.org/10.3390/app151910303.